Post-Print

M. Tillotson Rudd, M.R. Schultz, N.W. Gardner, C.J. R. Kosztowny, C. Bisagni
Analysis and Testing of a Launch-Vehicle-like Composite Conical–cylindrical Shell
AIAA Journal, Vol. 62, N. 9, 2024, p. 3526-3543
doi:10.2514/1.j063617

Analysis and Testing of a Launch-Vehicle-Like Composite Conical-Cylindrical Shell

Michelle Tillotson Rudd*
NASA Marshall Space Flight Center, Huntsville, AL, 35812, USA

Marc R. Schultz,† Nathaniel W. Gardner,‡ and Cyrus J. R. Kosztowny§
NASA Langley Research Center, Hampton, VA 23681, USA

Chiara Bisagni**
Politecnico di Milano, Milan, 20156, Italy

Launch-vehicle shell structures, which can be comprised of both cylindrical and conical sections, are known to be susceptible to buckling due to their large radius-to-thickness ratios. Advancements in composite manufacturing and numerical methods have enabled designers to consider more nontraditional shapes, such as connecting the conical and cylindrical sections with a toroidal transition to create a single-piece conical-cylindrical shell. This single-piece construction eliminates the need for a stiff, heavy interface ring between sections and has the potential to reduce mass. To better understand the buckling behavior of a composite conical-cylindrical shell, a lab-scale article was designed, fabricated, and tested. Prior to test, a finite element model that included thickness variations and radial imperfections was created. The test article buckled elastically at 251.8 kN, approximately 8.8% higher than the predicted buckling load of 231.4 kN. Because the test article buckled elastically, the buckling test was repeated. The measured buckling load from the second test was within 1% of the first.

---

* Aerospace Engineer, Structural Design, Development, and Analysis Branch, EV32, AIAA Member.
† Research Aerospace Engineer, Structural Mechanics and Concepts Branch, MS 190, AIAA Associate Fellow.
‡ Research Aerospace Engineer, Structural Dynamics Branch, MS 190.
§ Research Aerospace Engineer, Structural Mechanics and Concepts Branch, MS 190.
** Professor, Department of Aerospace Science and Technology, Milan, Italy and Guest Professor at Delft University of Technology, Faculty of Aerospace Engineering, Delft, The Netherlands, AIAA Fellow; chiara.bisagni@polimi.it.

Continued research in conical-cylindrical structures has the potential to expand the design space for launch-vehicle structures and lead to improved designs and reduce mass.

Nomenclature

3CHELL = *Composite conical-cylindrical shell test article*
AFP = *Automated fiber placement*
DIC = *Digital image correlation*
dX = *Relative displacement in the X direction*
dY = *Relative displacement in the Y direction*
dZ = *Relative displacement in the Z direction*
f = *Natural frequency*
FEM = *Finite element model*
GNA = *Geometrically nonlinear analysis*
IML = *Inner mold line*
LBA = *Linear bifurcation analysis*
LVDT = *Linear variable differential transformer*
l = *Longitudinal surface coordinate on a flattened cone*
MSFC = *Marshall Space Flight Center*
OML = *Outer mold line*
SLS = *Space Launch System*
Sylda = *Système de Lancement Double Ariane*
r = *Radius*
USA = *Universal Stage Adapter*
X = *Position, positive towards 3CHELL 0-degree circumferential location*
Y = *Position, positive towards 3CHELL 90-degree circumferential location*
Z = *Axial position along the center of rotation of 3CHELL*
A = *Rayleigh mass proportional damping*
B = *Rayleigh stiffness proportional damping*

Φ = *Circumferential surface coordinate on a flattened cone*

α = *Semi-vertex angle*

ξ = *Damping coefficient*

ϕ = *Nominal fiber angle*

θ = *Circumferential location*

I. Introduction

Conical and cylindrical shells are common geometric configurations in launch vehicles. The cylindrical shape is a main component of launch vehicles due to its high strength-to-volume ratio. Conical sections are utilized when transitioning from different-diameter cylindrical components such as the transition between first and second stages, as in the Launch Vehicle Stage Adapter on the first NASA Space Launch System (SLS) configuration, Block 1, as shown in Figure 1[1]. They are also employed for payload adapters which are nested within the launch vehicle. For conical and cylindrical structures, buckling, due in part to the high-axial compressive loads the launch vehicle is required to support during ascent, is one of the possible failure modes and consequently is an important consideration in design. Buckling may also significantly influence the design of launch vehicles and payload adapters that consist of unitized or combined conical and cylindrical shells.

Figure 1. NASA SLS Block 1 configuration.

Traditional launch-vehicle designs that rely on traditional manufacturing methods typically use heavy circumferential rings to join conical and cylindrical structures. Advances in composite manufacturing, such as automated fiber placement (AFP), and numerical tools, such as finite element codes, enable aerospace engineers to consider alternative designs. These designs may include combining the conical and cylindrical components to create a unitized conical-cylindrical shell with a toroidal transition for launch-vehicle structures and payload adapters. This unitized configuration would eliminate the need for interface rings, which can potentially lead to significant mass savings. Examples of this type of construction are the SLS Universal Stage Adapter (USA), which is currently under development [2], Figure 2, the Système de Lancement Double Ariane (Sylda) on the Ariane 5, and Vega Secondary Payload Adapter [3].

Figure 2. The NASA Universal Stage Adapter.

Empirically based design factors, or knockdown factors, are often used to ensure adequate margin to prevent global buckling. Such empirically based buckling knockdown factors for cylinders are published in NASA SP-8007 [4] along with recommendations for developing analysis-based knockdown factors. NASA SP-8007 was originally published in 1965 and much of the experimental data presented was based on experimental results as early as the 1920s with little or no data from composite shells. There is a common consensus that the design factors are overly conservative, which has contributed to the underlying motivation of researchers to understand the buckling behavior of composite cylindrical shells specifically for launch-vehicle applications to save mass. For example, Hilburger and Starnes used high-fidelity models to predict the buckling response of composite shells to better understand the sensitivities of these structures to geometric imperfection because the current guidelines were known to be overly conservative due to the lack of data [5]. More recently, Takano, et al., tested composite cylindrical shells with a large radius-to-thickness ratio. The published experimental results for composite cylinders had only extended to a radius-to-thickness ratio of 500, while Takano, et al. tested shells with a ratio equal to 848 [6]. Rudd, et al. also tested a composite cylindrical shell and developed a high-fidelity finite element model including geometric imperfections to predict the buckling and postbuckling behavior to validate a numerical methodology with application to the design of launch vehicles [7]. Also, Hartwich, et al. published experimental data about how different manufacturing methods and boundary conditions can affect the buckling results of composite shells [8]. Wagner, et al. have also contributed to the body of knowledge pertaining to the buckling of composite cylinders to improve the designs of launch vehicle structures by suggesting approaches to determine lower-bound knockdown factors [9].

Large projects have been established by the European Union and NASA to address the conservativism in the buckling design guidelines. In 2012 the New Robust DESIgn Guideline for Imperfection Sensitive COmposite Launcher Structures (DESICOS) project was established. A goal for the DESICOS project was to determine analysis methods to confidently provide less conservative, lower-bound knockdown factors for the design of composite cylindrical launch-vehicle structures. The DESICOS researchers used analytical, numerical, experimental, and probabilistic techniques [10]. The NASA Shell Buckling Knockdown Factor project has published a series of papers documenting the test and analysis of 2.4-m-diameter composite sandwich cylindrical shells with the intent to help define a modeling methodology to develop design-specific knockdown factors for composite sandwich cylindrical shells [11-13]. In summary, researchers have cited the need to further investigate the buckling behavior of composite cylindrical shells to improve the design of these structures for aerospace applications.

A similar pattern is also witnessed as a motivation for studying composite cones. A monograph with design recommendations for the buckling of thin-walled conical shells, NASA SP-8019 [14], was published shortly after NASA SP-8007. NASA SP-8019 recommends using a buckling knockdown factor of 0.33 for thin-walled conical shells, and has similar shortcomings as NASA SP-8007. The guidance given in SP-8019 was based on much less data than the guidance in SP-8007 for cylindrical shells. Therefore, researchers have started building a knowledge base for the buckling of conical shells that is similar to cylindrical shells. For example, Tong published experimental results on the buckling of nine carbon-fiber-reinforced-plastic and nine glass-fiber-reinforced-plastic conical shells with the aim of adding to the limited amount of research available at that time [15]. Goldfeld and Arbocz studied the imperfection sensitivity of laminated conical shells [16]. Khakimova, et al., developed high-fidelity finite element models (FEMs) to predict the buckling behavior of three carbon-fiber-reinforced-polymer conical shells; this FEM included features such as midsurface radial imperfections and thickness data. The goal of Khakimova, et al. research was to address the fact that composite materials were not included when developing NASA SP-8019 [17, 18]. In support of the DESICOS project, Ambrovich, et al., tested two cylindrical and two conical shells [19]. More recently, Sleight, et al. documented the results from an imperfection sensitivity study for conical sandwich-composite structures for launch vehicles [20]. One of the main objectives for each of the cited papers is to address the need for more research for buckling critical composite conical shells to improve future launch vehicle and payload adapter designs.

The buckling behavior of conical-cylindrical shells has been studied by researchers using numerical and semi-analytical methods, but the research was primarily aimed at civil engineering and piping applications. Wunderluich, et al., developed a semi-analytical approach to perform a nonlinear static and dynamic analysis of isotropic pressure vessels. In their research, Wunderluich, et al. investigated toriconical shells, meaning either a conical or spherical end, connected to a cylindrical base with a toroidal segment between [21]. Anwen published a paper on the buckling of a conical-cylindrical structure with a toroidal transition segment but assumed isotropic material properties and only considered external pressure loading [22]. To date, Patel, et al., and Singh and Patel have published research on the buckling and postbuckling characteristics of composite conical-cylindrical shells subjected to torsion, external pressure, axial compression, and thermal loading [23, 24]. Interrogated in their research were the effects of layup, cone angle, and axisymmetric imperfections, but they did not consider a toroidal transition, and the boundary conditions assumed were more in-line with the civil engineering and piping applications. Zarei and Rahimi published a study regarding the buckling resistance of joined composite conical-cylindrical shells, but again toroidal transitions were not considered, and they focused on lateral pressure loading [25].

Minimal experimental data has been published for conical-cylindrical structures, and the majority of the data is related to metallic structures. Hu and Raney tested a metallic conical-cylindrical shell to validate their analytical models for vibration response, but not global buckling [26]. Bushnell and Galletly, and Zhao tested to failure structures similar to those of Hu and Raney under internal pressure to validate finite element methodologies [27, 28]. Chronopoulos, et al., developed a numerical model to predict the vibroacoustic response of a composite conical-cylindrical-conical shell, which was a scaled down Sylda on the Ariane 5 [29].

More generally, the conical-cylindrical shell shape can be classified as a shell of revolution or shell with variable curvatures. There have been a numerous publications dedicated to numerical and analytical methods to determine the buckling load of shells of revolutions and shells of variable curvature. For example, Marguerre published a technical memorandum on the stability of variable curvature shells [30]. Also, a series of NASA contractor reports with analysis methods for stress and stability for shells of revolution were published [31-33] where the imperfection sensitivity under external pressure was studied. Though the structural application is different, the geometry is similar. Also, Tornabene and Viola and Tornabene, et al., researched the response of functionally graded doubly-curved shells [34, 35], specifically, the static response and free vibration. More recently, Zingoni and Enoma studied the strength and stability of spherical-conical shells, which would be pressurized and used in underwater applications [36].

The common goal for research published to-date on the buckling behavior of composite cylindrical and conical shells is addressing the lack of data available for these structures by publishing numerical and experimental test results. It has been realized that this data is vital to improve launch-vehicle and payload adapter designs. The application of unitized composite conical-cylindrical shells has potential to improve the mass efficiency of launch-vehicle primary and secondary structures by eliminating the need for the heavy interface rings that traditionally join the cylindrical and conical portions. To make this unitized conical-cylindrical shape a common design solution, it is necessary to have experimental data on the buckling of composite conical-cylindrical shells. To the authors' knowledge, there is currently no publicly available experimental data on the buckling of composite conical-cylindrical shells with toroidal transitions. To address this lack of experimental data, a composite conical-cylindrical shell was designed, built, and tested in axial compression until buckling failure with the objective of influencing and improving the designs of future aerospace structures.

First, in section II, the composite conical-cylindrical shell test article design and manufacturing will be discussed. The various nondestructive evaluation methods to determine the structural integrity of the part and collect data on the as-built configuration of the test article are discussed in Section III. The experimental setup is described in section IV. Finally, the results of the test and a comparison of the test data to the finite element model are discussed in Section V.

II. Test Article Design and Manufacturing

A composite conical-cylindrical shell test article, referred to herein as 3CHELL (Figure 3), was fabricated with Hexcel IM7/8552-1* (190 gsm) carbon fiber epoxy system. The test-article geometry is an approximate scaled-down version of the SLS USA. The overall height (axial length) of 3CHELL is 762 mm. The cylindrical inner mold line

---

*The use of trademarks or names of manufacturers in this report is for accurate reporting and does not constitute an official endorsement, either expressed or implied, of such products or manufacturers by the National Aeronautics and Space Administration.

(IML) diameter is 639 mm, and the IML diameter of the top of the conical shell is 418 mm. The conical shell has a 15-degree semi-vertex angle, α. The conical shell and cylindrical shell are combined with a seamless toroidal transition with a 380-mm radius of curvature.

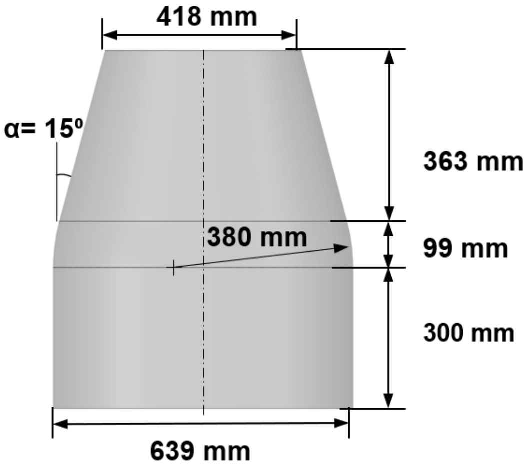

Figure 3. Test article geometry.

The test article was fabricated at the NASA Marshall Space Flight Center (MSFC) Composite Technology Center using the AFP robot. Unidirectional tows, 6.35-mm wide and nominally 0.183-mm thick, were laid on an aluminum mandrel that matched the inner mold line (IML) of the test article. The selected layup is quasi-isotropic with a nominal stacking sequence of $[45/-45/90/0]_S$ and a nominal laminate thickness of 1.46 mm, where 0 degrees is parallel to the axis of rotation and 90 degrees is perpendicular to the axis of rotation and tangential to the circular cross section of the shell that axial position. The positive ply angle is specified as clockwise from the 0-degree location when viewed from the outside. Figure 4 shows 3CHELL being manufactured at MSFC.

Figure 4. Test article being manufactured with the MSFC AFP robot.

The material properties for Hexcel IM7/8552-1 (190 gsm) were taken from data published by the National Institute for Aviation Research [37]. The lamina properties, such as elastic moduli and Poisson's ratio, are presented in Table 1. The B-basis laminate failure strength properties and laminate modulus for a layup with 25/50/25 proportion of 0-degree, 45-degree, and 90-degree plies are presented in the first two columns of Table 2. Failure strains were calculated from the laminate strength and modulus values assuming a linear elastic behavior and were used to design 3CHELL to have buckling occur prior to any strength failures under axial compression loading.

Table 1. Nominal lamina properties of Hexcel IM7/8552-1 composite.

0-degree modulus E_{11} (GPa)	90-degree modulus E_{22} (GPa)	Shear modulus G_{12} (GPa)	Poisson's ratio ν_{12} (-)
140.9	9.72	4.69	0.356

Table 2. Documented B-basis laminate failure stresses and calculated failure strains.

Test	Failure stress (MPa)	Modulus (GPa)	Calculated failure strain (με)
Unnotched tension	633.8	57.85	10,956
Unnotched compression	491.3	54.19	-9065

After the test article was fabricated, the upper and lower edges were trimmed flat and parallel to an overall final height of 813 mm with a final trimmed weight of 3.40 kg. Following trimming, each end of the test article was potted in aluminum end rings with 25.4-mm-deep channels, which left a free length of 762 mm. The test article was centered in the end rings and held in place with a ring of epoxy potting compound 8.0 mm wide on the outer mold line (OML) and 10.9 mm wide on the inner mold line (IML). The end rings were machined from an aluminum plate with an assumed modulus of elasticity of 71.01 GPa and Poisson's ratio of 0.33 [38]. The epoxy potting compound had an assumed modulus of elasticity of 7.58 GPa with an assumed Poisson's ratio of 0.33 [39]. The potted test article in the end rings is shown in Figure 5.

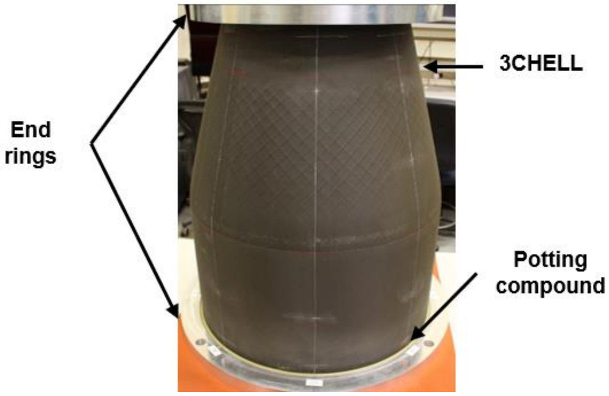

Figure 5. Test article potted in the end rings.

III. Nondestructive Evaluation

Thermography and structured light scanning were two nondestructive evaluation techniques used to assess the construction quality of 3CHELL prior to testing. Thermography was used to interrogate the integrity of the test article. The purpose of structured light scanning was to collect data on the as-built test article to better understand how radial imperfections and thickness variations affect the buckling response.

A. Thermography

Flash thermography was used to inspect the composite shell for flaws. A pulse of light is aimed at an area of interest and thermal diffusivity can be determined. A flaw, or indication, can be identified if there is a discontinuity in the thermal diffusivity in the area of interest. From this inspection, four areas of interest were noted in the cylindrical shell. The locations and sizes of the indications are given in Table 3. These areas were marked on 3CHELL to monitor during testing. Three of the four areas are located near the midheight of the cylinder, and the fourth is located near the cylinder end. No concerning areas were noted in the transition region or the conical section.

Table 3. Areas of interest identified with thermography.

Indication Number	Axial location from potted cylinder end (mm)	Circumferential location (degrees)	Approximate size (mm)
1	193	50°	8.0 × 5.0
2	188	93°	4.3 × 4.3
3	Encased in potting	210°	2.0 × 5.8
4	203	356°	13.5 × 6.4

B. Structured Light Scanning

Once 3CHELL was potted in the aluminum end rings, the geometries of the OML and IML were measured using structured light scanning, a photogrammetric technique [40]. The radial imperfections of the OML and IML are shown in Figure 6a, and the thickness calculated from the OML and IML data is shown in Figure 6b. The radial imperfections of the OML and IML ranged from a minimum inward radial deviation of 0.81 mm of the nominal surface to a maximum outward radial deviation of 1.01 mm of the nominal surface. The average thickness in the cylindrical and transition region of the shell was 1.37 mm. This would result in an average ply thickness of 0.171 mm, which is 6.5% less than the nominal ply thickness. In the conical section, a pattern of ±45-degree thickness variations that was due to tow overlaps is apparent. The overlapped region has a maximum thickness of 1.91 mm, and it is the result of the AFP process to maintain a constant angle and the choice to eliminate gaps between each course. A tow drop occurred approximately 140 mm from the conical top end, which accounts for the thickness discontinuity in the conical shell section. The patterns of overlaps and the thickness discontinuity are also apparent in Figure 5.

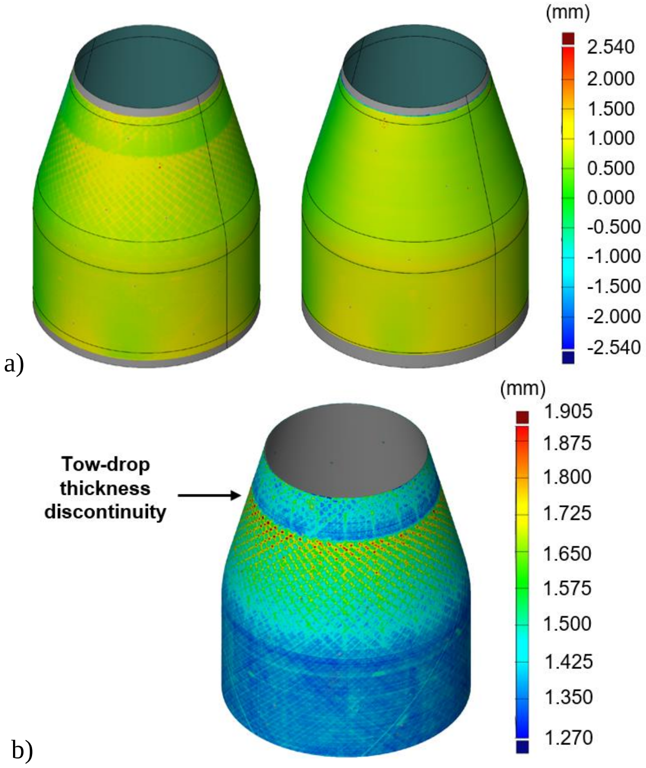

Figure 6. Structured light scan data of 3CHELL: a) Radial imperfections from OML (left) and IML (right); b) Measured thickness.

IV. Experimental Setup

The experimental setup was designed to capture the structural response, specifically the buckling behavior, of a composite conical-cylindrical shell under axial compression. The test article, 3CHELL, was highly instrumented and was subjected to several subcritical load sequences prior to the final load sequence to failure. These subcritical loads were 20% and 40% of the predicted 276.0-kN buckling load obtained from a geometrically nonlinear analysis (GNA) of the nominal test article with no radial or thickness imperfections. The final load case was to load 3CHELL to buckling. Testing was performed at MSFC using a load frame that is capable of applying loads up to 1112 kN. A displacement-controlled compression rate of 0.076 mm/min was used for all load sequences. Numerous data-collection sensors such as strain gages, linear variable differential transformers (LVDTs), and low-speed and high-speed digital image correlation (DIC) systems were used to monitor the test article prebuckling, buckling, and postbuckling response throughout all load sequences. An overview of the test setup and a closeup-view of 3CHELL in the load frame can be seen in Figure 7.

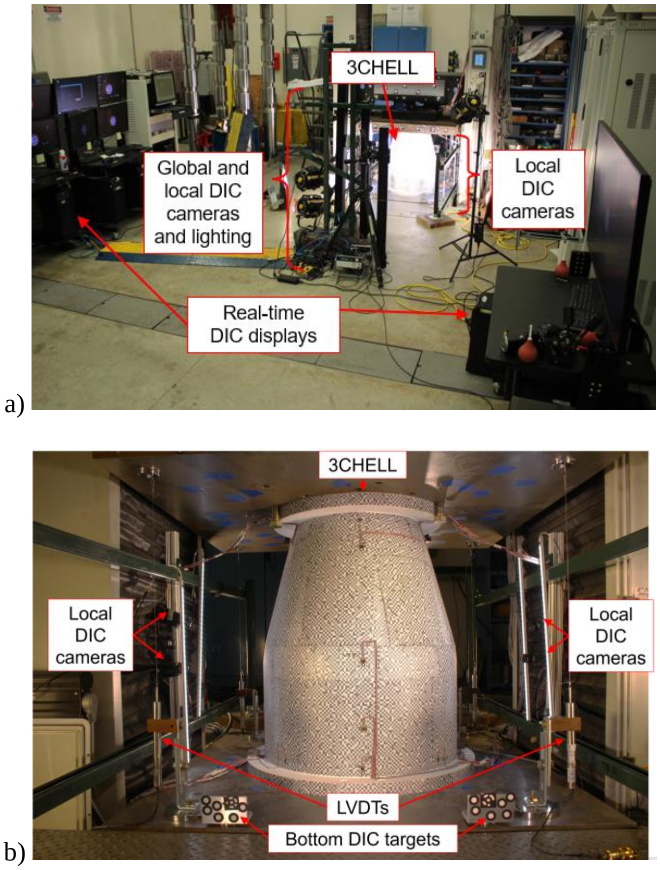

**Figure 7. Test setup of 3CHELL: a) Overview of test setup;
b) Close-up-view of 3CHELL in load frame.**

Strain gage data was used to monitor the behavior of the test article in real time and for postprocessing. A series of 16 IML and 16 OML uniaxial strain gages, measuring axial strain, were placed back-to-back and spaced every 45 degrees. Half of those strain gages were located 25.4 mm from the top end ring, and the remaining half were positioned 25.4 mm from bottom end ring. In addition, 24 back-to-back biaxial gages, measuring axial and hoop strain, were placed every 90 degrees at three different axial positions. The first set of biaxial gages were placed at the midheight of the cylindrical section, the second were placed near the center of the transition region, and the third were placed just above the tow drop in the conical section. A schematic of the strain gage layout is presented in Figure 8. The gages at the conical end, 25.4 mm away from the end ring, are referred to as the cone-end gages. The gages 101 mm from the ring are referred to as the cone midheight gages. The gages at the transition region are referred to as transition gages. A similar naming convention is applied to the cylinder gages 137 mm from the cylinder end ring and 25.4 mm from the cylinder ring, which are referred to as the cylinder midheight and cylinder end gages, respectively.

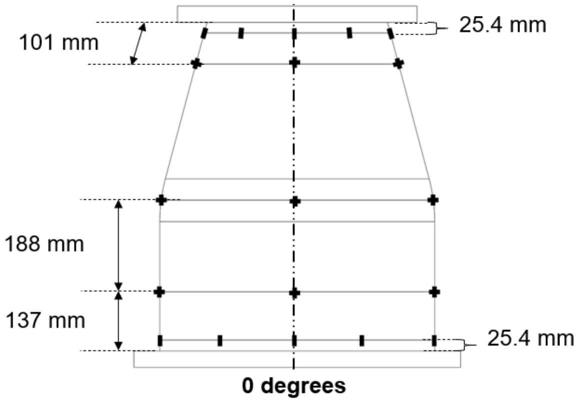

Figure 8. Strain gage layout.

Six pairs of low-speed DIC cameras (six low-speed DIC systems) and two pairs of high-speed DIC cameras (two high-speed DIC systems) were used to capture full-field displacements and strains. A top-down view of the DIC camera layout with approximate fields-of-view is shown in Figure 9. Of the low-speed DIC systems, the two systems centered about 0 and 180 degrees were used to measure the global behavior. Global refers to a field-of-view, approximately 711 mm x 864 mm, that includes the entire test article and end rings. The low-speed cameras had a capture rate of 1 Hz. Based on results obtained by the finite element analysis with perfect geometry, high strain gradients were expected at the transition region. Therefore, four low-speed local DIC systems were set up at 0, 90, 180, and 270 degrees, with a field of view to focus on the transition region between the conical and cylindrical section. The fields of view of these local systems were approximately 297 mm x 365 mm. The local systems provided a higher resolution to measure the deformations and strains more accurately in this area of interest.

The high-speed systems were also placed at 0 and 180 degrees with a similar global field-of-view and a frame rate of 10,000 Hz. The high-speed cameras were intended to capture the entire buckling event from just prior to buckling initiation (incipient) through buckling propagation and postbuckling. The system was triggered by an operator when buckling was observed either audibly or visually, and the images from when the system was triggered to approximately 2.5 seconds before the trigger were saved.

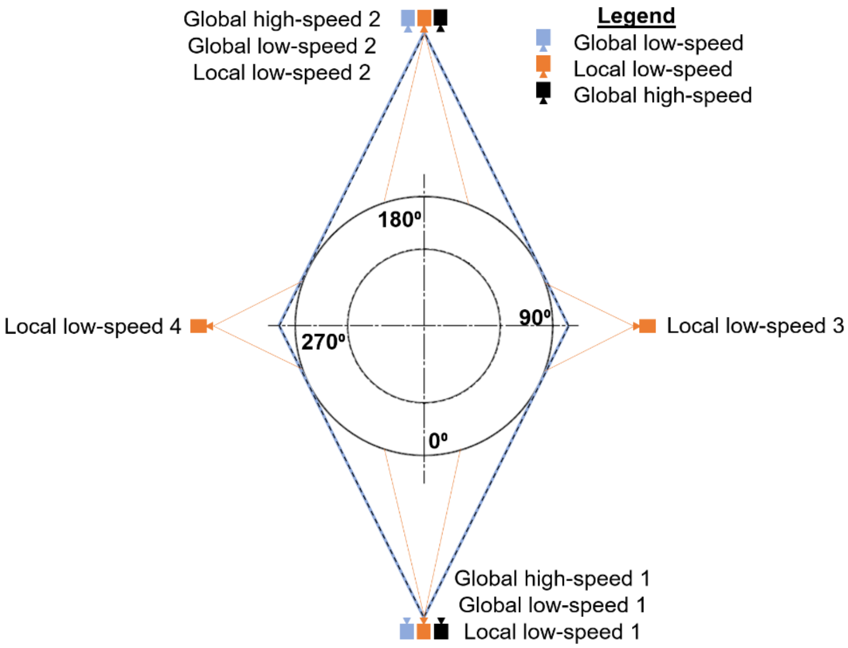

Figure 9. Top-down view of the DIC camera layout with approximate fields-of view.

The high-contrast speckle pattern for DIC accommodated both the low-speed (global and local) and the high-speed (global) photogrammetry requirements, which are based on camera resolution, acquisition rate, and field of view. A speckle size of 6.4 mm was utilized for the global systems, while a speckle size 1/10 of the global size was considered more appropriate for the local systems. To accommodate both speckle sizes in a single pattern, the entire test article was covered with a pattern similar to that shown in Figure 10, where it is seen that there is a two-tiered speckle pattern. The larger squares represent the speckle pattern that was utilized by the global systems, and the smaller squares within the larger squares represent the speckle pattern that was utilized by the local systems. The pattern was printed on transfer paper and then applied to the test article. This technique was first demonstrated by Bomarito, et al. [41,42] on small specimens, and has also been applied to a large-scale buckling test [13].

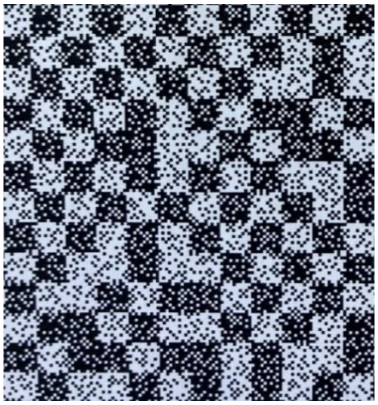

Figure 10. Example of the DIC speckle pattern for 3CHELL.

Four LVDTs were placed at the four corners of the load frame to measure relative axial displacements of the loading platens. To measure movement perpendicular to the loading direction, four targets were placed on the top and bottom corners of the load platens. These targets were monitored by a ninth DIC system to measure the movement of these points and can be seen in Figure 7.

V. Results and Discussion

In this section, a description of the FEM used to predict the buckling response of 3CHELL is presented. A comparison of the test data to the predicted response is then provided. A discussion of the off-nominal loading observed during the test, and how this anomaly affected the predicted response, is presented next. Finally, the results of the repeated experimental buckling load sequence are presented. Results of the test article behavior at incipient buckling and postbuckling are discussed in detail.

A. Finite element model and analysis

A FEM of 3CHELL was created using Abaqus 2021 [43]. The four-node, reduced-integration shell element, S4R, was selected to characterize the solid laminate, potting compound, and end rings.

The tow drop was not a specifically desired design feature, but instead was an artifact of the AFP manufacturing process where the changes in the shell geometry result in tow gaps and/or tow overlaps. During the shell design process, it was decided to not allow tow gaps, so changes in shell geometry resulted in tow overlaps. According to the measured thickness variation in Figure 6b, the laminate had areas where the thickness was almost 40% thicker than the acreage laminate thickness of 1.37 mm. Therefore, it was important to incorporate the tow-overlap and tow-drop features into the FEM. To discretely model the thickness variations of the ply overlaps the equation of the fiber path for a constant angle on a conical surface,

$$\Phi(l) = \tan\phi \ln\left[\frac{l}{l_0}\right] + \Phi_0 \tag{1}$$

was used [44]. In the equation, Φ is the circumferential coordinate on an unrolled, flattened cone, ϕ is the nominal fiber angle, l_0 is the distance from the conical apex to the top edge of the cone which is derived from the small end radius (r_0), and l is the longitudinal surface coordinate on a flattened cone that can be calculated by the radius (r). The flattened cone configuration and variables associated with equation 1 is presented in Figure 11.

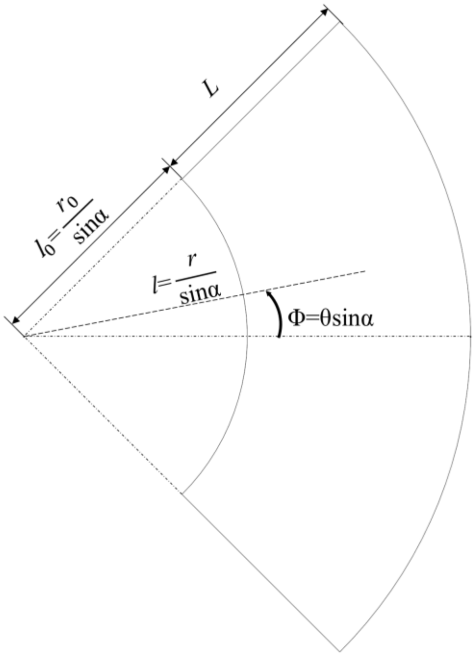

Figure 11. Flattened cone configuration.

The FEM with a detailed view of the thickness variations is presented in Figure 12. The cyan color represents the acreage or nominal layup, the light gray areas represent the end regions that are surrounded by the potting compound and end rings, the red color represents where two +45-degree plies overlap, the yellow color represents where two -45-degree plies overlap, and the dark blue region represents where the overlapped positive and negative 45-degree tows intersect. The positive X-axis of the FEM aligns with the 0-degree circumferential location, the positive Y-axis aligns with the 90-degree circumferential location, and Z is defined along the axis of rotation.

During manufacturing, the amount of overlap in the +45 and -45 plies grew linearly as the diameter decreased until the point where one entire tow-width was overlapped, and a tow drop was instituted. The decision to section the overlapped area in the FEM into thirds (expanded section of Figure 12) was based on calculations comparing the density of various axial sections. The stacking sequences for the composite shell are given in Table 4, where the emboldened font indicates an overlapped ply.

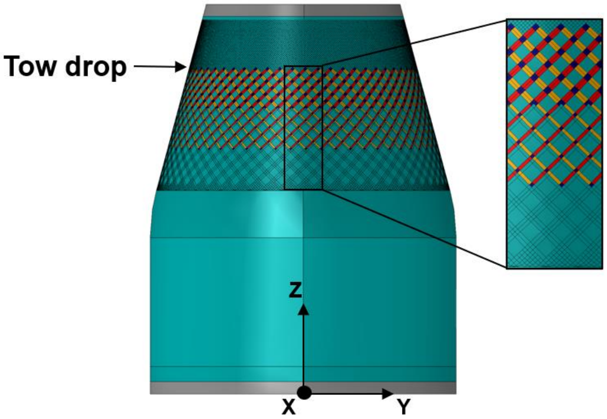

Figure 12. Finite element model with thickness-variation details.

Table 4. Section properties of the FEM.

Section	FEM color	Stacking Sequence
Acreage	Cyan	45/-45/90/0/0/90/-45/45
+45 overlap	Red	45/**45**/-45/90/0/0/90/-45/**45**/45
-45 overlap	Yellow	45/-45/**-45**/90/0/0/90/**-45**/-45/45
+45 and -45 overlap	Dark blue	45/**45**/-45/**-45**/90/0/0/90/**-45**/-45/**45**/45
Potted ends	Gray	Al ring/Potting/Acreage/Potting/Al ring

Explicitly modeling the ply overlaps in the geometry made meshing complex. A mesh convergence study was used to determine that an approximate mesh size of 5 mm was appropriate to capture the buckling behavior of the composite conical-cylindrical test article with a uniform mesh. A mesh size of 3.8 mm was utilized herein because the smaller mesh was necessary to incorporate the thickness variations.

After the model was meshed, the radial imperfections were incorporated. The IML structured light scan data was used as the source for the radial imperfections since the OML data had influences of the thickness variations. The process in which the radial imperfections were incorporated is explained by Kosztowny [45]. In addition, the measurement-derived average ply thickness of 0.171 mm was used in the FEM. The end-ring configuration in the test article was used to approximate a clamped boundary condition. To apply clamped boundary conditions, reference points were placed on the axis of rotation at the top and bottom and tie constraints were used to connect all degrees of freedom to the respective reference points. The bottom reference point had all degrees of freedom fixed, and the top reference point had all degrees of freedom fixed except for axial displacement.

Linear bifurcation analysis (LBA), vibration analysis, and implicit nonlinear transient analysis, referred to as GNA, were used to predict the structural response of 3CHELL. The Lanczos solver was used to determine the linear eigenvalues and modes. The critical eigenvalue was 307.8 kN from the LBA. To determine the damping parameters (the Rayleigh mass proportional damping, A, and the Rayleigh stiffness proportional damping, B) for the GNA, the first natural frequency, *f*, from a free vibration analysis was required. The equations for Rayleigh mass damping constant

$$A=2\pi f\xi\,, \tag{2}$$

and stiffness proportional damping constant

$$B=\frac{\xi}{2\pi f} \tag{3}$$

were calculated where the damping coefficient, ξ, of 0.05 was assumed.

For the GNA, the time integrator parameter of -0.05 was used for slight numerical damping as suggested by [43]. The half increment solution parameter was set equal to the approximate buckling load of 3CHELL. The transient dynamic analysis used a time duration of 2000 seconds, with an initial time increment and a maximum increment of 1 second each. An applied displacement was ramped linearly from 0.00 mm to -2.54 mm at the top reference node to obtain the load rate of 0.076 mm/min that was used in the test. This was completed in a single analysis step. The GNA was performed for the structure with and without geometric imperfections. The GNA without imperfections resulted in a buckling load of 246.7 kN, which is approximately 20% less than the linear eigenvalue buckling load of 307.8 kN. The GNA with imperfections resulted in a buckling load of 235.1 kN, which is approximately 24% less than the linear eigenvalue buckling load. The inclusion of imperfections reduced the GNA buckling load by 5%. Table 5 includes a summary of the analyses and results. It should also be mentioned that the incorporation of the thickness variations increased the LBA load by 12%.

Table 5. Summary of analysis results

Analysis type	Radial imperfections (Y/N)	Thickness variations (Y/N)	Buckling load (kN)
LBA	N	Y	307.8
GNA	N	Y	246.7
GNA	Y	Y	235.1

The FEM included much of the variances from the nominal design such as the tow overlaps and radial imperfections. The goal was to create a high-fidelity FEM to predict the buckling response of a composite conical-cylindrical. From this, a validated modeling approach could be used in future analyses for developing buckling design guidelines for composite conical-cylindrical shell.

B. Test-analysis correlation

The test article 3CHELL buckled at a load of 251.8 kN, 7.1% greater than the predicted nonlinear buckling load with radial imperfections of 235.1 kN. The load versus displacement curves for the predicted and measured behavior are shown in Figure 13. The end shortening data was determined using DIC by measuring the change in length between points on the top and bottom end rings. It is observed that the test article was approximately 14% stiffer than the FEM-predicted stiffness. There is also a notable change in slope that occurs around 50 kN. Additionally, the postbuckling equilibrium load predicted using the model was approximately 96.1 kN. The postbuckling equilibrium load during test was 96.6 kN.

The predicted radial displacements at incipient buckling are presented in Figure 14a. Multiple potential buckling-initiation sites can be observed as blue and black dimples just above the transition region with a minimum inward displacement of -0.42 mm. Another band of blue dimples is seen just below the transition in the cylindrical portion as well, but the minimum inward displacement in this region is only -0.08 mm. A third row of dimples, not as pronounced as the first two, is observed just above the tow-drop region. Ultimately, it was predicted that buckling would initiate with the dimple located at the 120-degree circumferential location in the cone just above the transition region. The outward radial displacement was predicted to be relatively uniform with the most-pronounced outward deformations shown in Figure 14a as the two red bands in the transition region. The maximum predicted outward radial displacement is 0.87 mm. Despite the presence of the radial imperfections, the radial displacements are relatively uniform at a given longitudinal location.

There are similarities between the predicted radial displacements, Figure 14a, and the observed radial displacements during test, Figure 14b. For example, the three sets of relatively inward radial displacements can be seen just above and below the transition region, and just above the tow drop. In addition, the region of the most outward deformation occurred in the transition region with a magnitude of 0.87 mm, the same as was predicted. On the other hand, the measured maximum inward displacement of -0.20 mm at incipient of buckling is approximately half of the predicted -0.42. There were also similarities in the axial location of the radial-displacement patterns, but the dimples in the cylindrical region were more prominent than those in the conical region in the test data while the dimples were predicted to be more prominent in the conical region. The measured radial displacements in the cone seem skewed in the X-Y plane at a given axial location, while in the displacement predictions are uniform. This skew can be identified globally in Figure 14 by the presence of the shades of green and light blue in the conical region in the figure centered about 0 degrees, and the dark blue and purple colors in the conical region in the figure centered about 180 degrees. More specifically, just above the tow-drop region at the 0-degree circumferential location the measured radial displacement is 0.44 mm. The measured radial displacement at 180 degrees at the same axial location is 0.13 mm.

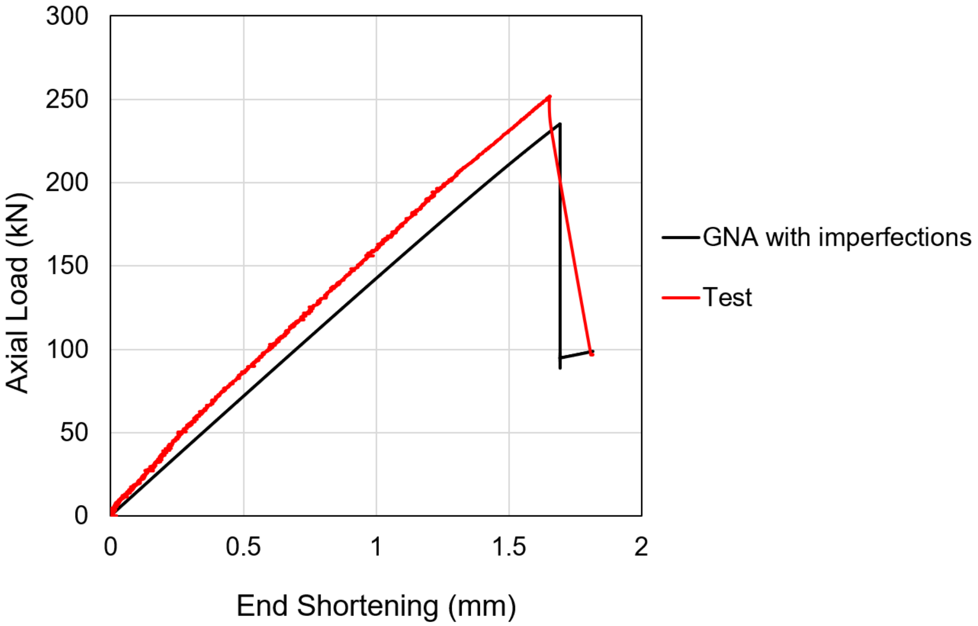

Figure 13. Axial load versus end shortening curve from the GNA and test.

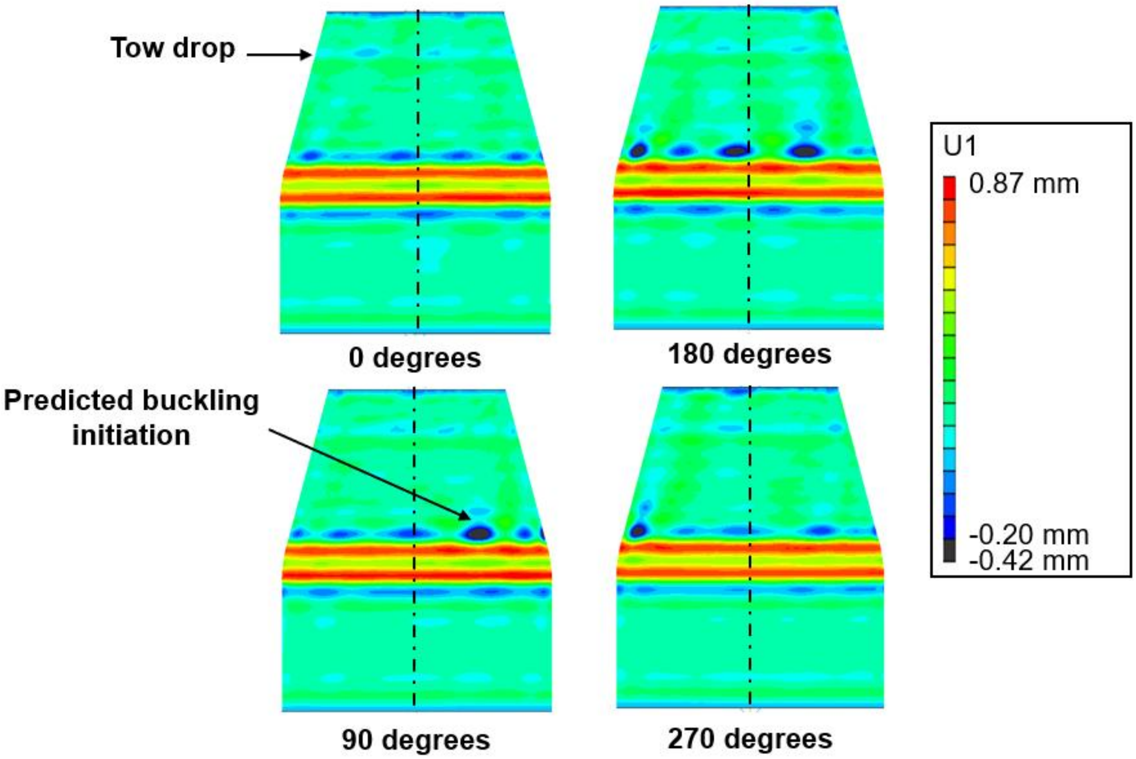

a)

b)

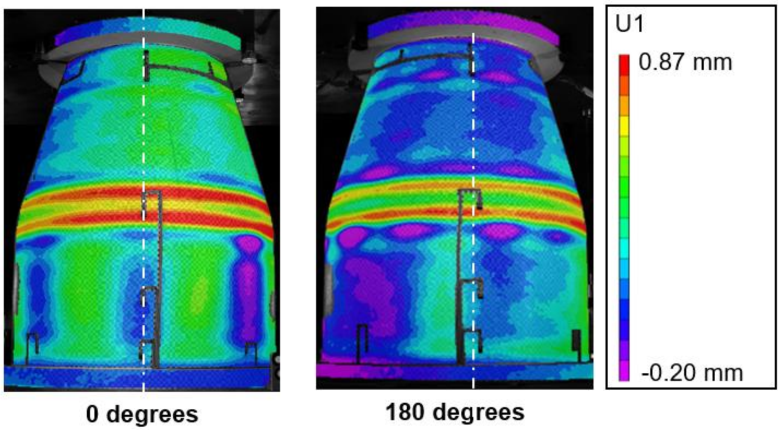

Figure 14. Radial displacement, U1, at incipient buckling: a) FEM; b) test.

It is suspected that buckling initiated in the cylinder just outside the field of view of the 180-degree-centered high-speed DIC system, which encompasses the circumferential coordinates of approximately 125 degrees to 235 degrees. Figure 15 shows the radial displacements measured with the high-speed DIC system at the time of buckling initiation, 1.6 milliseconds and 3.2 milliseconds into the buckling event, and in the final high-speed DIC frame at approximately 15 milliseconds. In the first high-speed image (buckling initiation, Figure 15a), there is a purple inward dimple that forms on the edge of the field of view, circled, with an inward displacement of -2.11 mm. Between the initial image and 1.6 milliseconds, the dimple grows slightly and begins to propagate, Figure 15b. After 3.2 milliseconds, the displacement at the buckling initiation location has grown much larger with an inward deformation approximately 6 times larger than it was at 1.6 milliseconds, Figure 15c. Also, adjacent to the buckling initiation dimple a pattern of four inward dimples has formed. Eventually, the four dimples coalesce into four circumferential axial waves around the entire cylindrical section of the specimen in the final post buckling configuration as shown in Figure 15d. The inward deformation of the post buckling configuration is -17.7 mm. The three dimples observed in the 180-degree high-speed camera view can also be viewed by 3CHELL in postbuckling as shown in Figure 16.

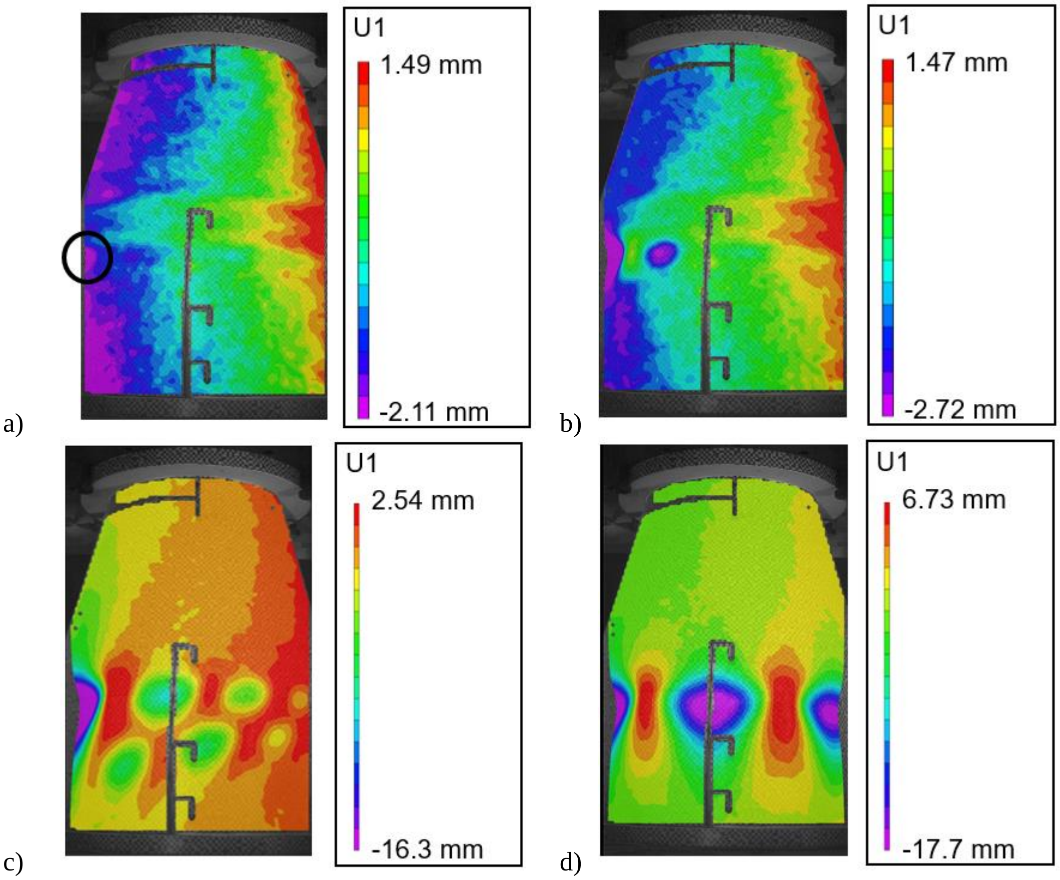

Figure 15. Buckling propagation from a) buckling initiation; b) 1.6 milliseconds after (a); c) 3.2 milliseconds after (a);and d) Postbuckling configuration.

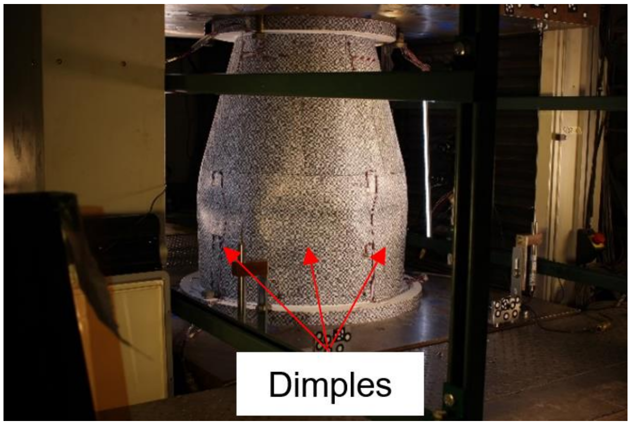

Figure 16. Postbuckling configuration of 3CHELL from the first test.

The high-speed images indicated that buckling initiated in the cylindrical portion of 3CHELL. However, buckling was predicted to initiate in the conical region, Figure 17. The postbuckling displacements from the FEM were taken from the point when the end-shortening in the analysis matched the measured test article end-shortening in a best attempt to quantitatively compare the data. Though the location of the predicted postbuckling deformation pattern is different than what was observed in test, the pattern and magnitude of inward and outward radial deformations is similar. The minimum predicted inward deformation was -16.8 mm, approximately 1.0 mm less than what was measured. The maximum outward predicted deformation in the postbuckling configuration was 7.52 mm, less than 1.0 mm greater than what was measured.

The differences between test and analysis in the postbuckling response is due, in part, to the assumptions made when including the thickness variations. Buckling was predicted to occur in the conical region and buckling propagation would remain in the conical region because conical region in FEM was not as stiff as the conical region in 3CHELL. Also, the differences between the number of dimples present could also be related to the thickness variations between 3CHELL and what was assumed in the FEM. With regards to stiffness, the predicted curve in Figure 13, shows a total loss of stiffness after buckling initiation, which is different from what was measured. The measured stiffness after the buckling event is related to the stiffness of the load frame.

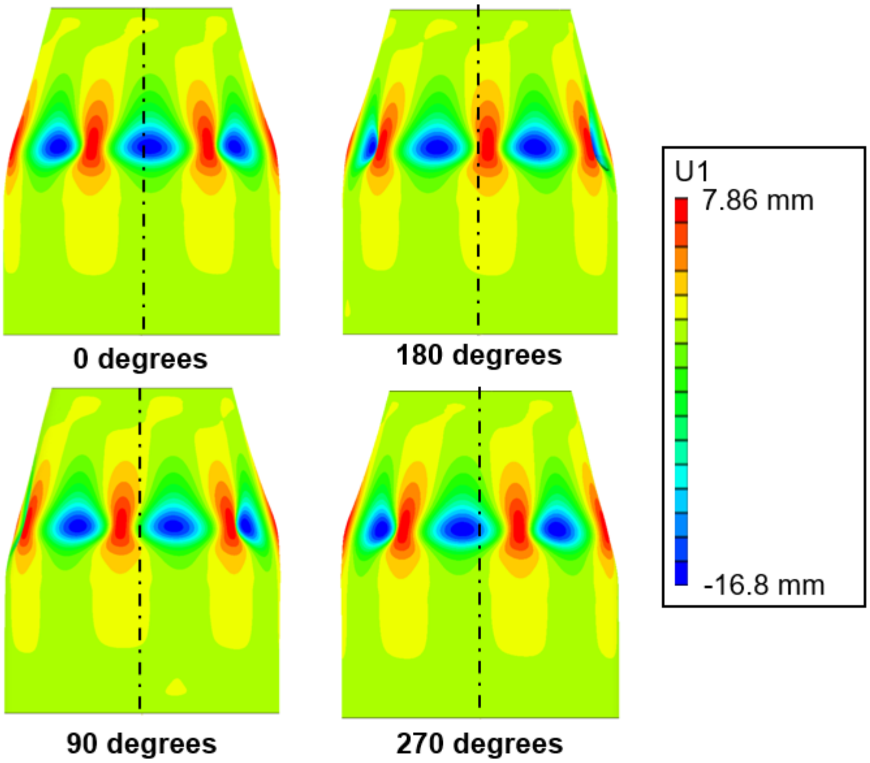

Figure 17. Postbuckling predicted by the FEM.

C. Posttest analysis

During testing, a small shearing motion in the load platen was identified using the real-time DIC displays. After the test the relative movement between the top and bottom end rings was measured using the coordinate system with respect to the load frame and the orientation of 3CHELL shown in Figure 18. The measurement dX and dY is the change in lateral displacement of the top load platen relative to the bottom load platen in the X direction (toward 0 degrees) and Y direction (toward 90 degrees). The DIC-measured relative displacement between the top and bottom end rings in the X and Y direction is shown Figure 19. It can be observed from this figure that the relative displacement between the top and bottom end rings at buckling was 0.16 mm in the X direction and 0.31 mm in the Y direction. This displacement results in a magnitude of 0.35 mm towards the 62-degree circumferential location. The total axial displacement of the test article at buckling was 1.65 mm, so the in-plane displacement was approximately 20% of the total axial shortening.

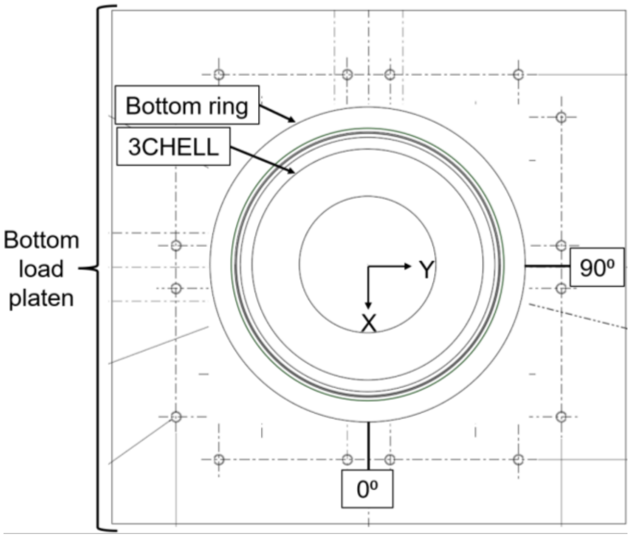

Figure 18. Top-down view of 3CHELL in load frame with coordinates for load platen movement.

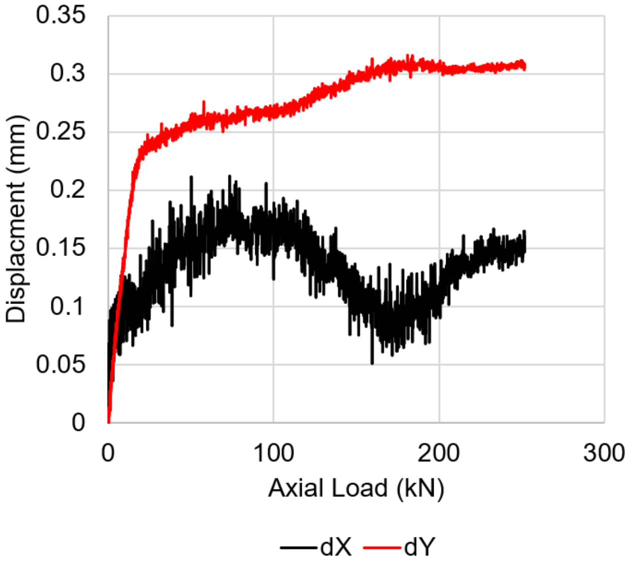

Figure 19. Measured load platen movement.

To represent the measured off-nominal shear displacement in the finite element analysis, an additional step was created in the analysis. The first step was used to simulate the relative shear displacements at buckling initiation of 0.16 mm in the X direction and 0.31 mm in the Y direction. The second step was used to simulate the application of the axial displacement at a rate of 0.076 mm/min, the same as used in the initial analysis.

The predicted buckling load with the shear displacement included was 231.4 kN, which is almost 2% lower than the initial FEM prediction and 8.8% lower than the experimental buckling load. In the load-versus-displacement curves in Figure 20, it can be observed that the stiffnesses of the FEM with and without the shear displacement are indistinguishable, but that the predicted buckling load with the included shear displacement is slightly lower. While there was minimal change in the overall response, a skewed pattern in the predicted radial displacements at incipient buckling is observed in the conical region due to the shear displacement in Figure 21. The predicted outward radial displacements with the shear displacement included were to 1.0 mm, higher than without the shear displacement, but the maximum inward radial displacement remained unchanged. The inclusion of shear displacement did not significantly influence the results, despite the fact that the magnitude of the shear displacement was 20% of the total end shortening. It should be noted that the postbuckling equilibrium load with shear is 96.7 kN, almost the same as the model without shear and the test postbuckling equilibrium load.

Some of the differences between test and analysis may be attributable to the assumptions made when incorporating the thickness variations into the FEM. The calculated specimen weight in the FEM was 3.31 kg and the measured weight of 3CHELL was 3.40 kg. The larger mass in the physical test article indicates that there was additional material not accounted for in the FEM. It is presumed that this additional material was related to the tow overlaps that form the grid-like pattern seen in the thickness variations in Figure 6b, and may be the reason for the measured stiffness being higher than predicted, and subsequently the overall buckling load as well. In addition, if the cone was stiffer than what was modeled and the cone was stiffer than the cylindrical region then this would explain the discrepancy in buckling location between the test and FEM. The difference between the test and analysis highlights the amount of detail that may be required to accurately capture the buckling behavior of a conical-cylindrical shell. The buckling behavior of conical-cylindrical shells may be sensitive to stiffness variations (e.g., tow overlaps) intentional or otherwise.

In the future, importing the thickness data from the structured light scan data into the FEM could help improve the results, and a smaller mesh size. An attempt was made to include the structured light scanning data into the finite element model using the continuum shell reduced integration elements (SC8R) and a smaller mesh edge side of 2.54

mm. The OML and IML nodes could be manipulated based on the structured light scanning data from the OML and IML surfaces and could account for the radial imperfections and thickness variations. Afterwards, the section properties for elements with an increase thickness corresponding to an additional ply would need to be modified. Unfortunately, this approach made the model computationally cumbersome. The model took about an hour to load. . This approach was not implemented due to time constraints. A similar approach of modifying the SC8R nodes to account for thickness and radial imperfections to predict the buckling of a composite cylinder is presented in reference 7 with good results.

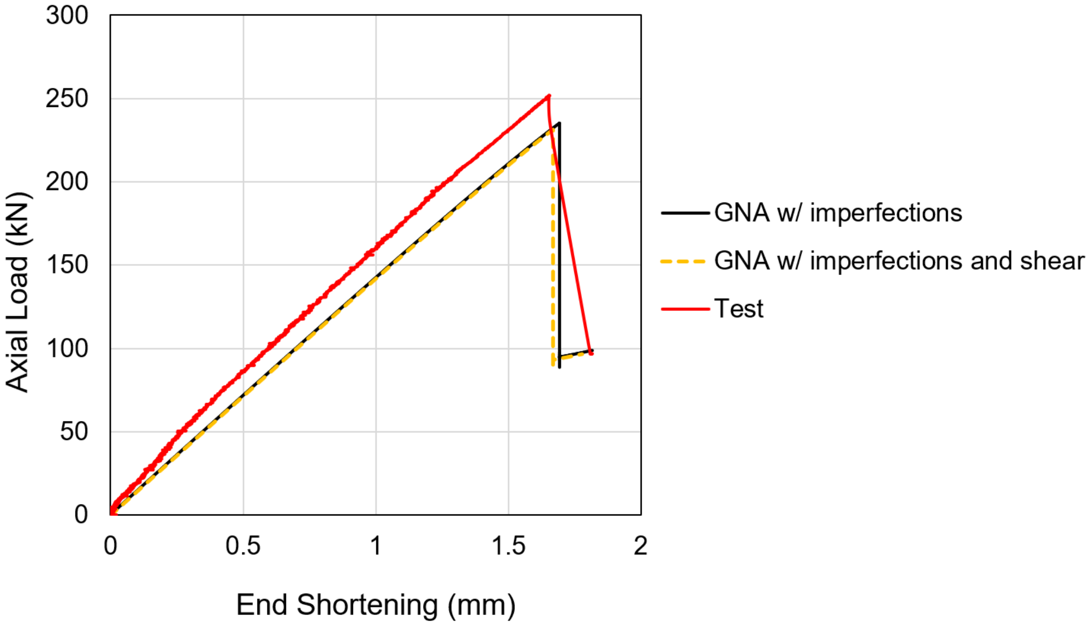

Figure 20. Axial load versus end shortening curve from the GNA with shear and without shear, and test.

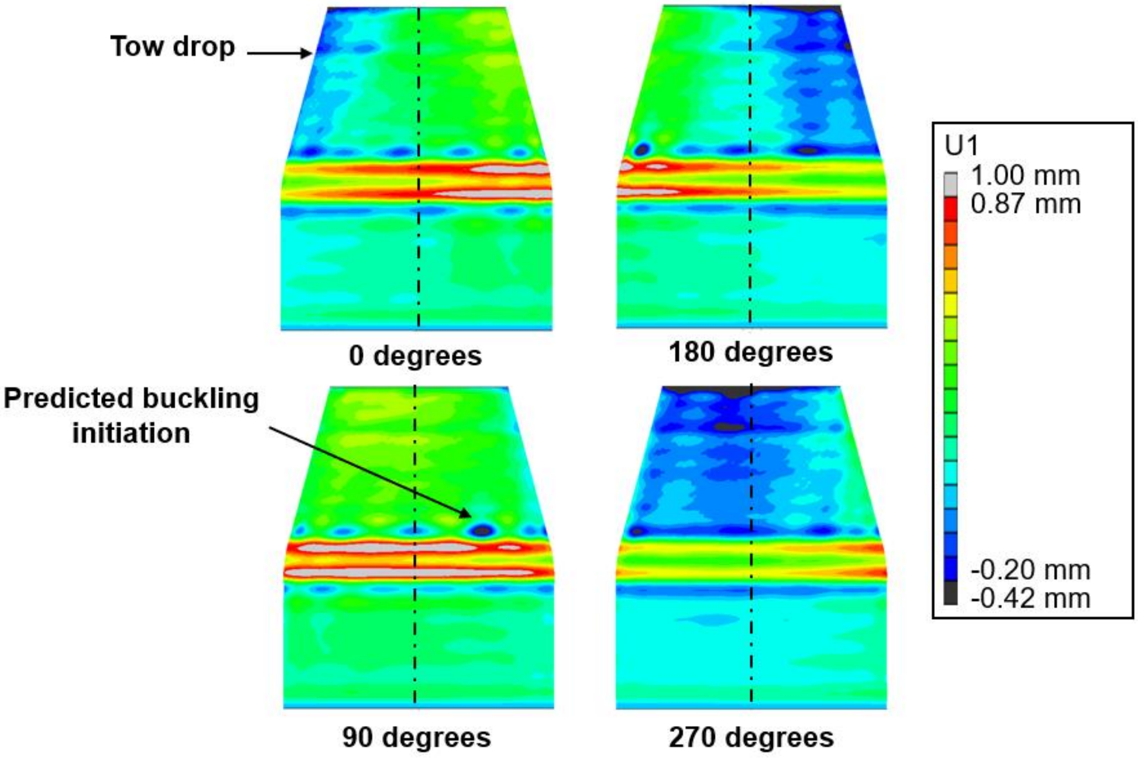

Figure 21. FEM with shear radial displacements at incipient buckling.

The full-field strain distribution from DIC can be compared to the strain from the outermost ply in the FEM with the shear displacement. The predicted and measured maximum principal strains are presented in Figure 22 and Figure 23, respectively. The patterns and strain magnitudes are quite similar for the views centered about 0 degrees (Figure 22a and Figure 23a) and 180 degrees (Figure 22b and Figure 23b). The maximum principal direction is primarily in the hoop direction. The areas with the highest maximum principal strain are in the transition region and coincide with the areas of maximum radial displacement. The highest predicted maximum principal strain at incipient buckling was 2785 με. This value is within 3% of the measured highest maximum principal strain of 2853 με.

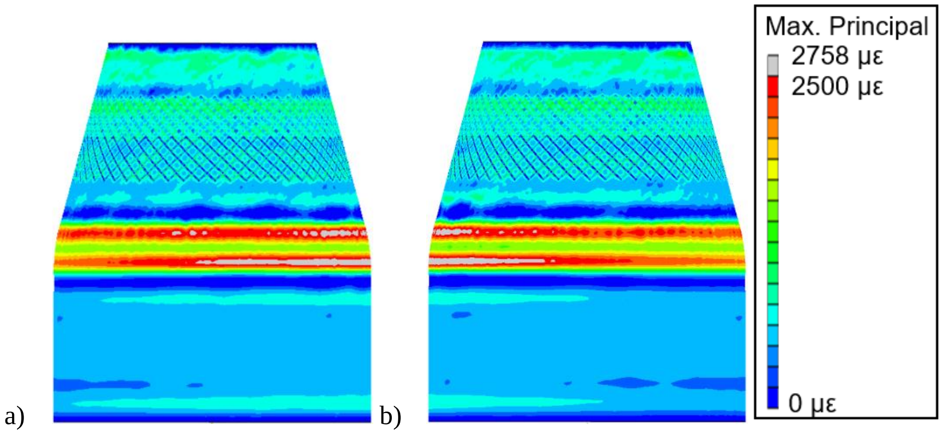

**Figure 22. Predicted maximum principal strain at incipient buckling:
a) centered at 0 degrees; b) centered at 180 degrees.**

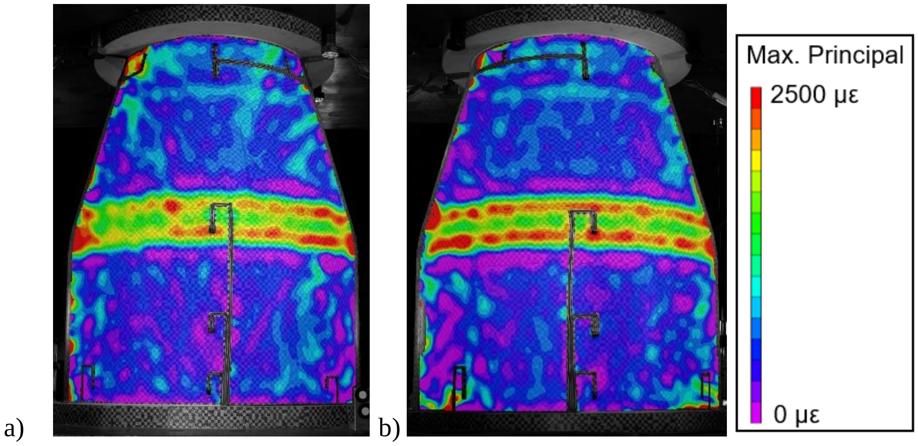

**Figure 23. Measured maximum principal strain at incipient buckling:
a) centered at 0 degrees; b) centered at 180 degrees.**

There are also elements of agreement when comparing the predicted and measured minimum principal strains as shown in Figure 24 and Figure 25. The minimum principal direction primarily corresponds to the axial direction. First, it is important to note the band of highly negative strains near the end of the conical region in the FEM. This predicted negative strain is due to the way in which the radial imperfections were incorporated into the model. The structured light scanning data near this region is noisy, which can lead to abrupt radial changes in the mesh. The lowest predicted minimum principal recorded in this region is -7131 με. If this end region is discounted, then the lowest minimum principal strain is -4222 με, which occurs just above the transition region at the base of the cone in Figure 24b. This spot corresponds to the inward dimple in Figure 21 for the view centered about 180 degrees. The lowest minimum principal strain measured at incipient buckling was -3971 με, which occurs in roughly the same circumferential region as was predicted, but just below the transition in the cylinder. As with the maximum principal strain plots, the ply overlaps are observed in the predicted data, but not in the DIC data.

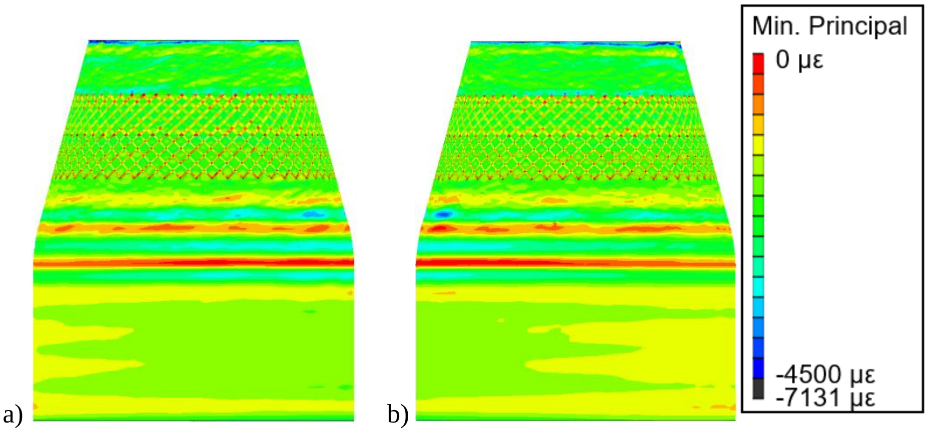

Figure 24. Predicted minimum principal strain incipient of buckling: a) centered at 0 degrees; b) centered at 180 degrees.

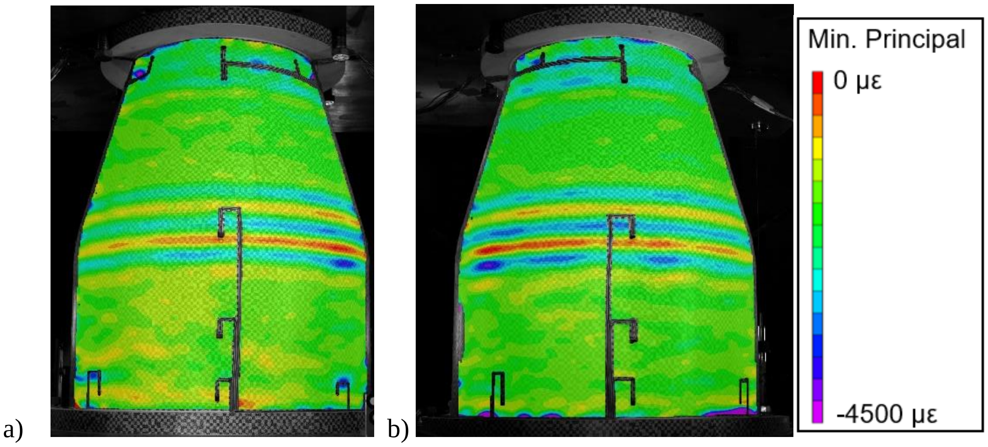

Figure 25. Measured minimum principal strain at incipient buckling: a) centered at 0 degrees; b) centered at 180 degrees.

The predicted and measured cylindrical-end axial membrane strains, shown in Figure 26, and bending strains, shown in Figure 27, were plotted to investigate the previously mentioned experimental slope change observed in the load versus displacement plot, Figure 13 and Figure 20. A slope-change behavior can also be observed in the cylinder-end axial membrane strain at the 0-degree circumferential location, black solid line (Figure 26a). Also, change in stiffness can be seen in the 45-degree circumferential location at approximately 25 kN where the slope is increasing until just under 50 kN when the slope decreases slightly (Figure 26b). In the bending-strain data at the cylindrical end, there is no calculated bending strain until just below 50 kN for the 0-degree and 45-degree circumferential degree locations (Figure 27a and b). The change in slope around 50 kN may be related to the bending strain.

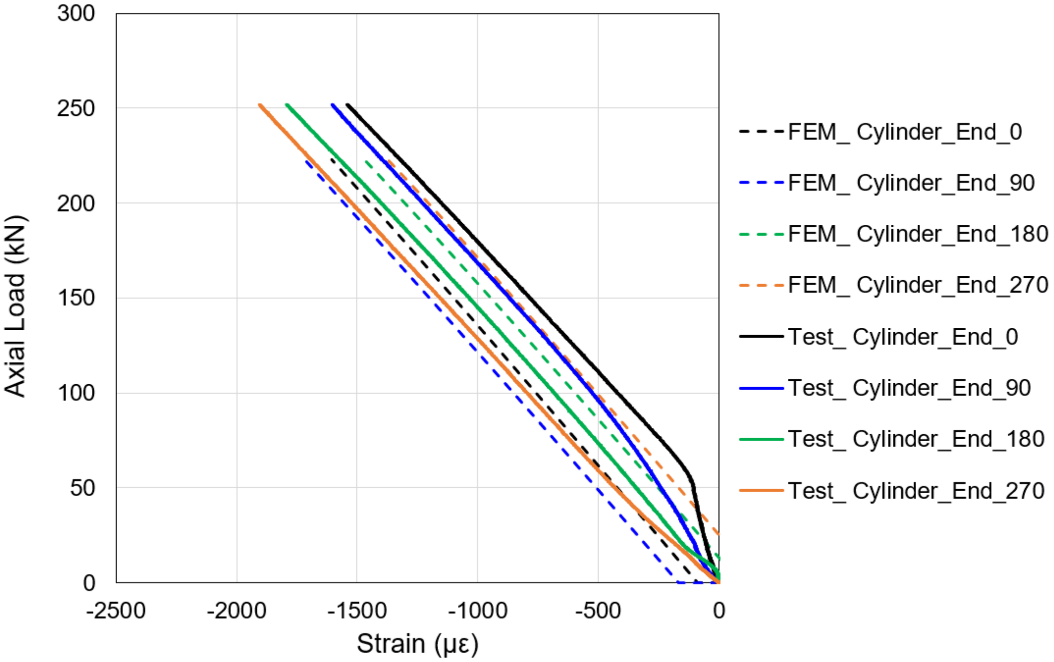

a)

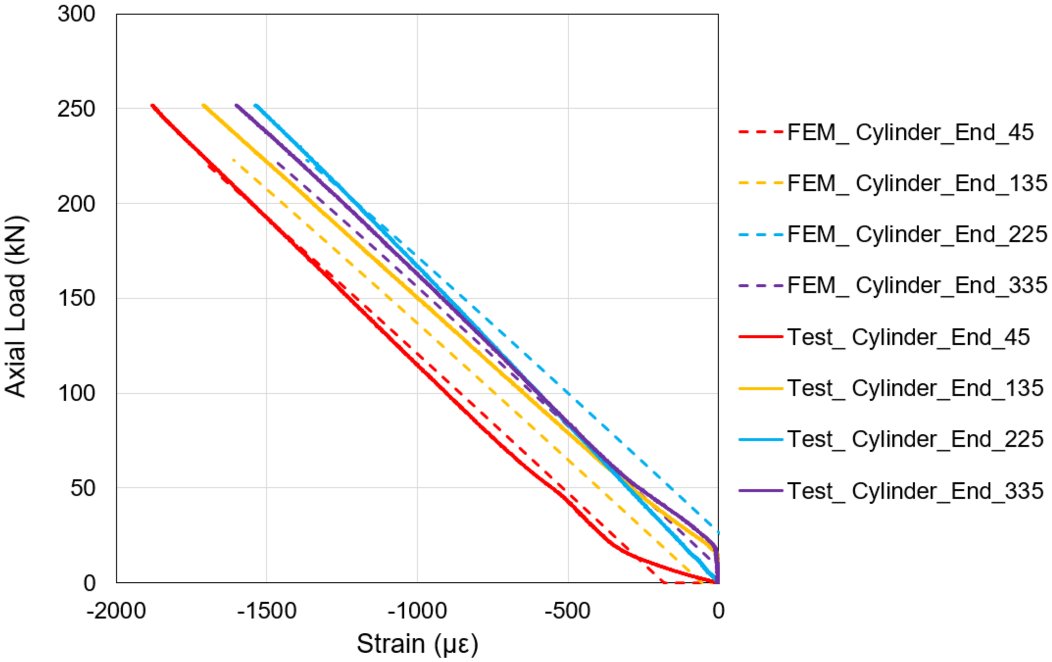

b)

Figure 26. Cylinder-end axial membrane strains: a) 0-, 90-, 180-, and 270-degree locations; b) 45-, 135-, 225-, and 335-degree locations.

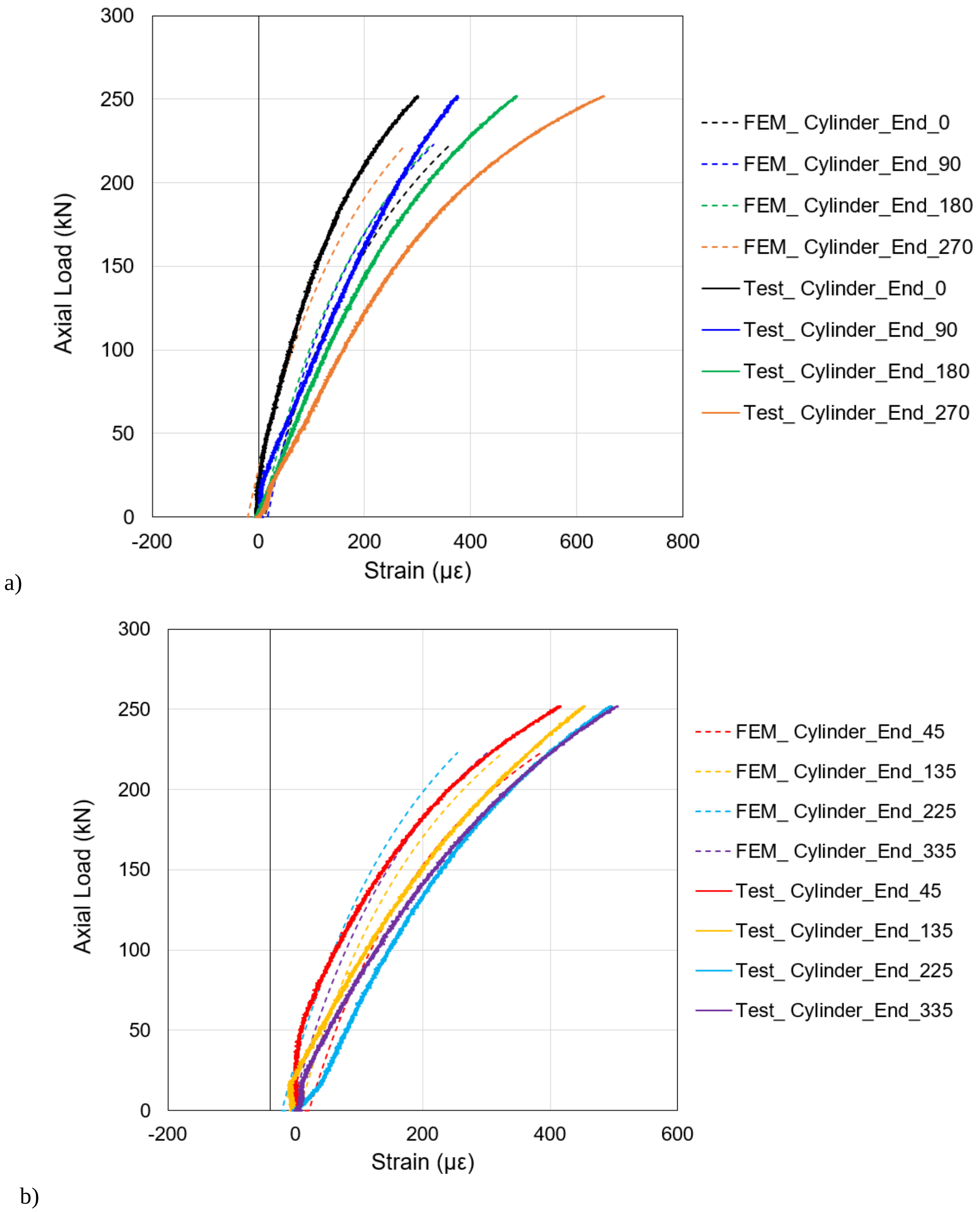

Figure 27. Cylinder-end bending strains: a) 0-, 90-, 180-, and 270-degree locations; b) 45-, 135-, 225-, and 335-degree locations.

To better understand why the cylinder-end bending strain at 0 degrees remains near zero until a load of approximately 50 kN, DIC was used to compare the change in axial displacement before and after 50 kN. Shown in Figure 28 is the change in axial displacement, dZ, between a) 10 kN and 20 kN, b) 20kN and 40 kN, c) 40 kN and 50 kN, and d) 50 kN and 70 kN for the DIC cameras centered about 0 degrees. Shown in Figure 29 is the change in axial displacement at the same load levels, but for the DIC cameras centered about 180 degrees. The change in axial displacement pattern between 10 kN and 20 kN was dominated by the shear displacement imparted by the load frame, and not due to the axial load, Figure 28a and Figure 29a. As the load increased, the top of the test article exhibited a more-uniform loading pattern as shown by the horizontal purple band with similar magnitudes in Figure 28b and Figure 29b. At the bottom of the test article at 0 degrees, there is more axial displacement than at the edges of the frame (towards 335 and 45 degrees) in Figure 28b. This variation in the bottom axial displacement is observed by the warmer colors near the edge of the frame that correspond to a smaller change in axial displacement compared to the cooler colors that represent a larger change in axial displacement near the center of the frame, Figure 28b. A more-uniform distribution is observed in the bottom of Figure 29b, where the relatively horizontal bands extend from the top to the bottom. This same trend of more bottom displacement-variation near the 0-degree position than the 180-degree position is seen in Figure 28c and Figure 29c, which show the change in axial displacement between 40 kN and 50 kN. This trend indicates a potential gap between the ring and end of the test article near 0 degrees, which would allow the test article to displace more in this region than at 335 and 45 degrees where the end of 3CHELL could be in contact with the end ring. The behavior was more uniform in the DIC system centered around the 180-degree circumferential location at the same load level, as indicated by the horizontal contour bands, signifying a more uniform axial displacement. Instead, the more uniform horizontal bands indicate more uniform axial displacement. Between 40 kN and 50 kN, the bottom edge of 3CHELL is lifted by 0.01 mm shown by the green-yellow coloration at the bottom end ring-test article interface in Figure 28 . After the slope change, the change in axial displacement between 50 and 70 kN becomes more uniform for the region centered about 0 degrees. The horizonal bands in Figures 28d and 29d are relatively uniform, which may signify that a gap has closed, and the test article is in complete contact with the ring. The change in axial displacement between 50 and 70 kN at 180 degrees remained uniform. The fact that the measured responses are more uniform in Figure 29 than in Figure 28 correlates well with the strain data because the slope change anomaly was most apparent in the cylinder gages at 0 degrees.

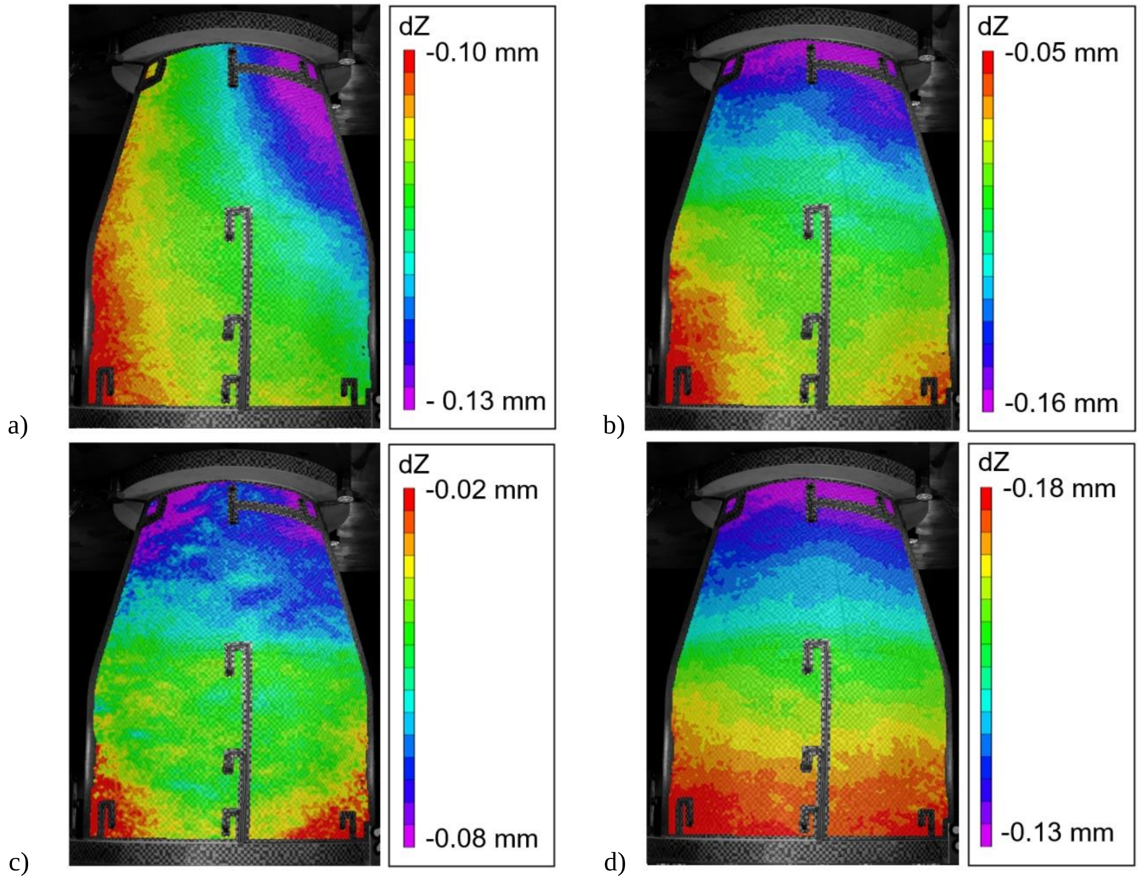

Figure 28. Change in axial displacement at 0-dgerees between load intervals: a) 10 kN-20 kN; b) 20 kN-40 kN; c) 40 kN-50 kN; d) 50 kN-70 kN

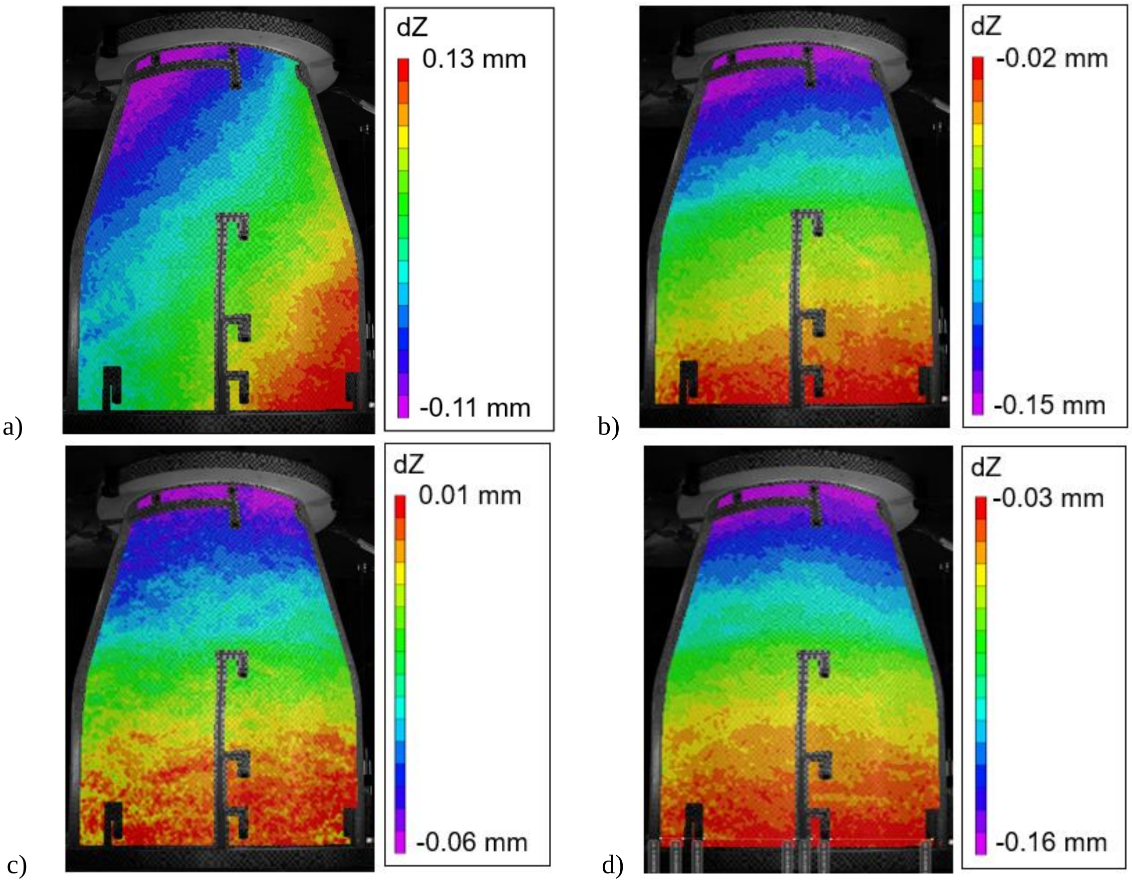

Figure 29. Change in axial displacement at 180-degrees between load intervals: a) 10 kN-20 kN; b) 20 kN-40 kN; c) 40 kN-50 kN; d) 50 kN-70 kN.

The maximum and minimum principal strains in the postbuckling pattern also have elements of agreement when comparing the test results to the FEM as shown in Figure 30- Figure 33 despite the fact that the buckling occurred in the cylindrical region rather than the conical region as predicted. The postbuckling strains from the FEM were taken from the point when the end-shortening in the analysis matched the measured test article end-shortening in an attempt to quantitatively compare the data. The maximum and minimum principal strain values predicted are quite similar to what was measured. The highest maximum principal strain predicted was 9020 με and the strain measured was 9055 με. This is only a 35 με difference which is within the error limits of the DIC capability. The region of maximum principal strain occurred between the dimples in the postbuckling configuration shown in Figure 30 and Figure 31. The most-negative minimum principal strain predicted was -9396 με. The most-negative minimum principal strain measured was -9613 με, less than 3% different from what was predicted, which occurs at the edges of the dimples in the postbuckling configuration, Figure 32 and Figure 33. The magnitudes of the strains are similar, even though postbuckling behavior was contained in the cylindrical region instead of the conical region as predicted. The difference in the postbuckling location is most likely due to the assumptions made when incorporating the thickness variations in FEM.

It should be noted the highest measured maximum principal strain of 9055 με is less than the threshold used in design as reported in Table 2 of (10,956 με). However, the lowest measured minimum principal strain value of -9613 με is greater than the design value of -9065 με. The calculated failure strains are conservative since they were calculated assuming linear elastic properties. After loading, the test article returned to its original shape, and no material failure was apparent upon visual inspection. Based on these observations, it was concluded that they test article may be undamaged, and it was decided to repeat the final load sequence.

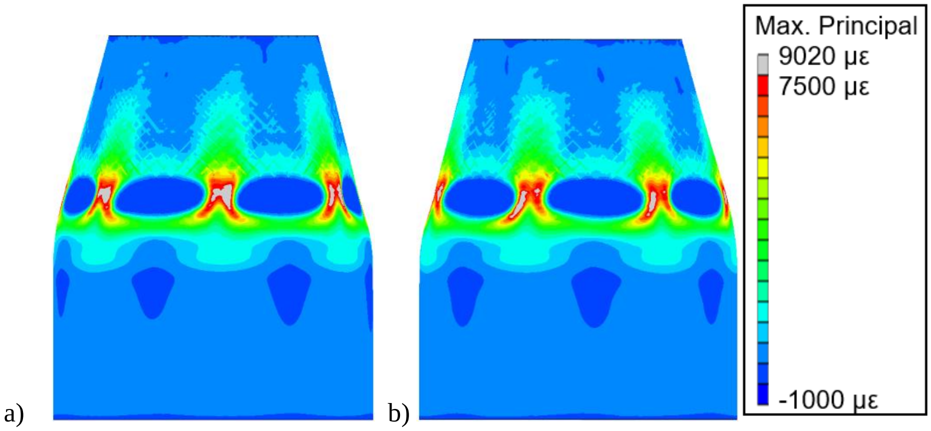

Figure 30. Predicted maximum principal strain at postbuckling: a) centered at 0 degrees; b) centered at 180 degrees.

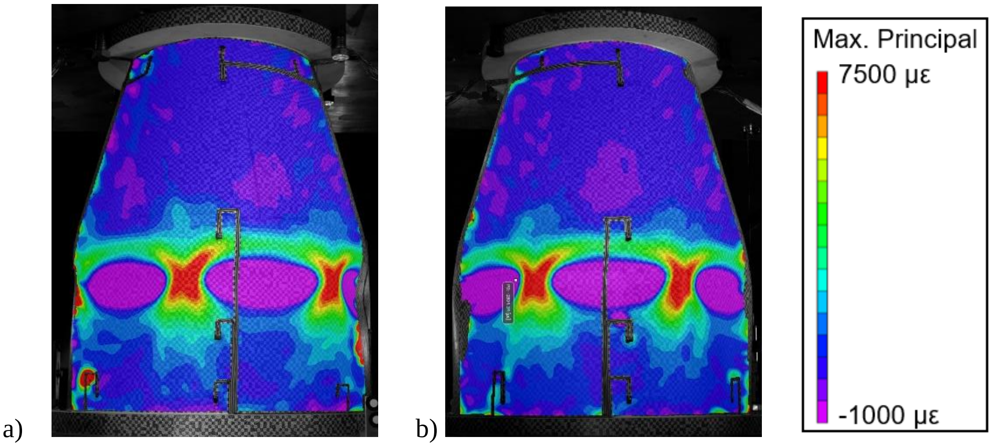

Figure 31. Measured maximum principal strain at postbuckling: a) centered at 0 degrees; b) centered at 180 degrees.

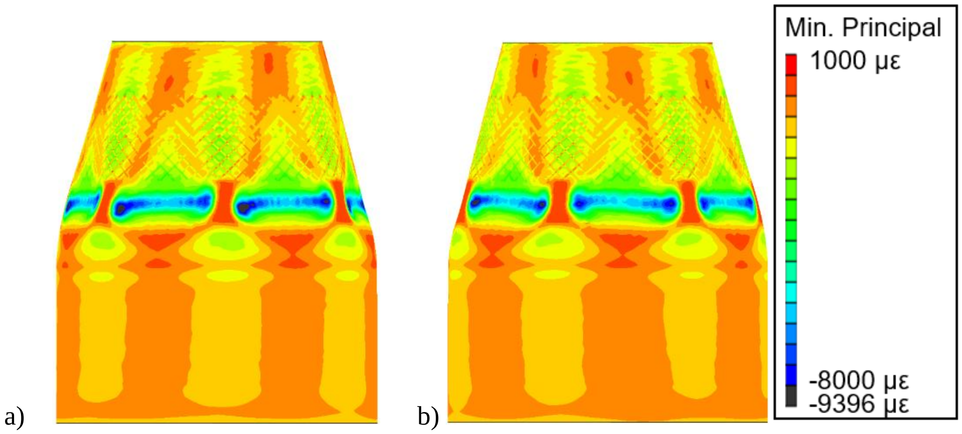

Figure 32. Predicted minimum principal strain at postbuckling:
a) centered at 0 degrees; b) centered at 180 degrees.

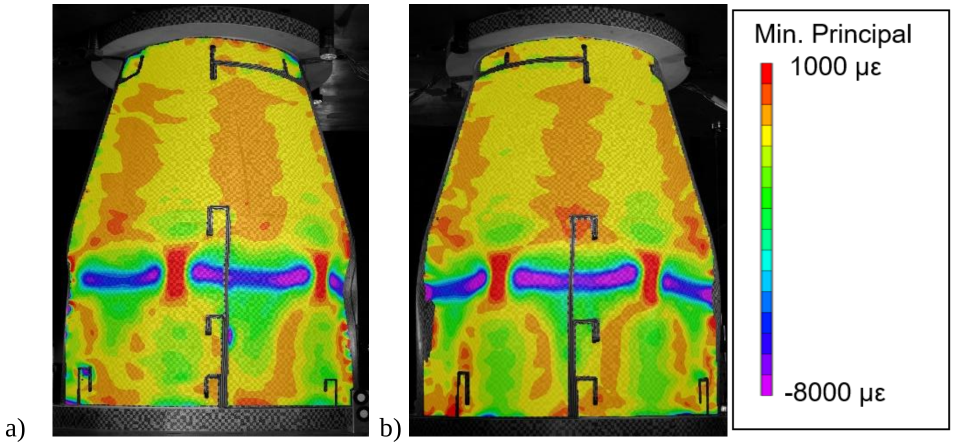

Figure 33. Measured minimum principal strain at postbuckling:
a) centered at 0 degrees; b) centered at 180 degrees.

Overall, there was good correlation between the FEM and the experimental results, which is valuable since there is limited experimental data on the buckling of composite conical-cylindrical shells. The differences between test and analysis may not necessarily be related to the modeling methodology, but rather external factors such as the test setup and model resolution related to the tow overlaps. For example, the shear from the load platen affected the radial displacements. Also, the apparent gap in the end ring seemed to influence the test article's initial stiffness. Another possible source of variance was related to the manufacturing process, specifically the overlaps. It is thought the effects of the overlaps were amplified due to the geometry of 3CHELL, specifically the small radius, but would most likely not have an effect on a larger shell structure. In general, the model was able to predict the global behavior with good accuracy. This would suggest the modeling approach present is appropriate for predicting the buckling response of a conical-cylindrical shell, and could potentially be used in finite element analyses to develop buckling design guidance.

D. Second buckling test

Since the first test was successful and the test article appeared to have buckled elastically, it was decided to repeat the final buckling load sequence. The test-article response was very similar to that of the first buckling test and the test article buckled within 1% of the first buckling test, Figure 34. The measured buckling load from the first test was 251.8 kN with a measured end shortening of 1.65 mm, and during the second test 3CHELL buckled at 250.99 kN with a measured end shortening of 1.63 mm. As seen in Figure 34, the stiffnesses were essentially the same; the blue line, representing the load versus displacement curve from the second test, seems to trace over the load versus displacement curve (red line) from the first test. The postbuckling equilibrium load for the second test was 96.6 kN, as compared to 96.7 kN for the first test.

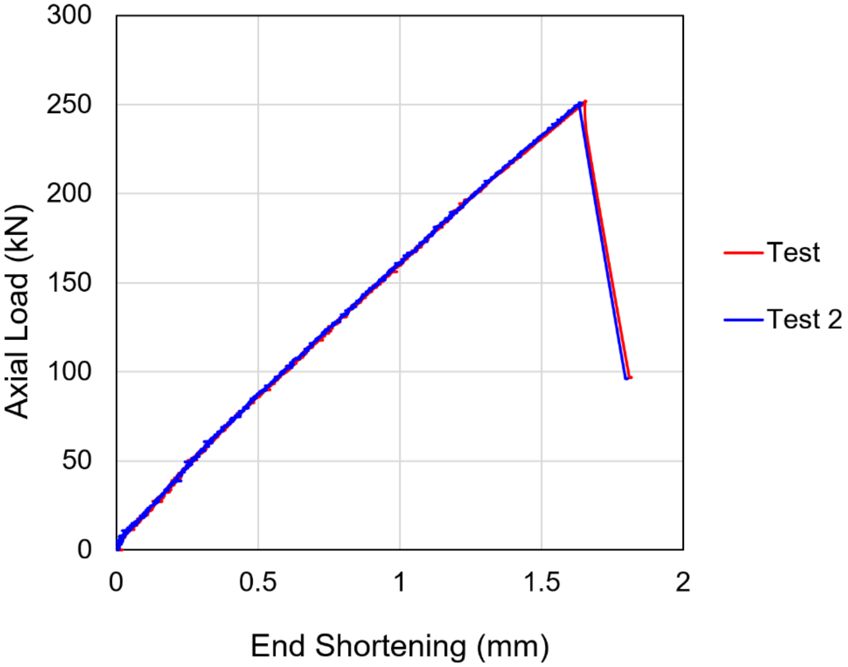

Figure 34. Axial load versus end shortening curve for both buckling load sequences.

The buckling propagation sequences from the first test, Figure 15, and the second test, Figure 35, were essentially the same. Buckling initiated in approximately the same region just outside the field of view of the high-speed camera, circled in Figure 15a and Figure 35a. A second dimple formed adjacent to the buckling initiation dimple 1.6 milliseconds after buckling initiation, Figure 15b and Figure 35b. In addition, two rows of dimples are present next to the buckling initiation after 3.2 milliseconds after buckling initiation, Figure 15c and Figure 35c. Finally, the postbuckling configuration of six circumferential waves is present in both the first and second test, Figure 15d and

Figure 35d. The outward and inward radial displacements for both postbuckling configurations are similar, where during the first test the maximum outward deformation was 6.73 mm and 7.24 mm during the second test. The maximum inward deformation was -17.7 mm and -17.8 mm after the first and second test, respectively. Similarly, three distinct dimples can be seen in the postbuckling configuration from the second test, Figure 36, as was observed in the first, Figure 16.

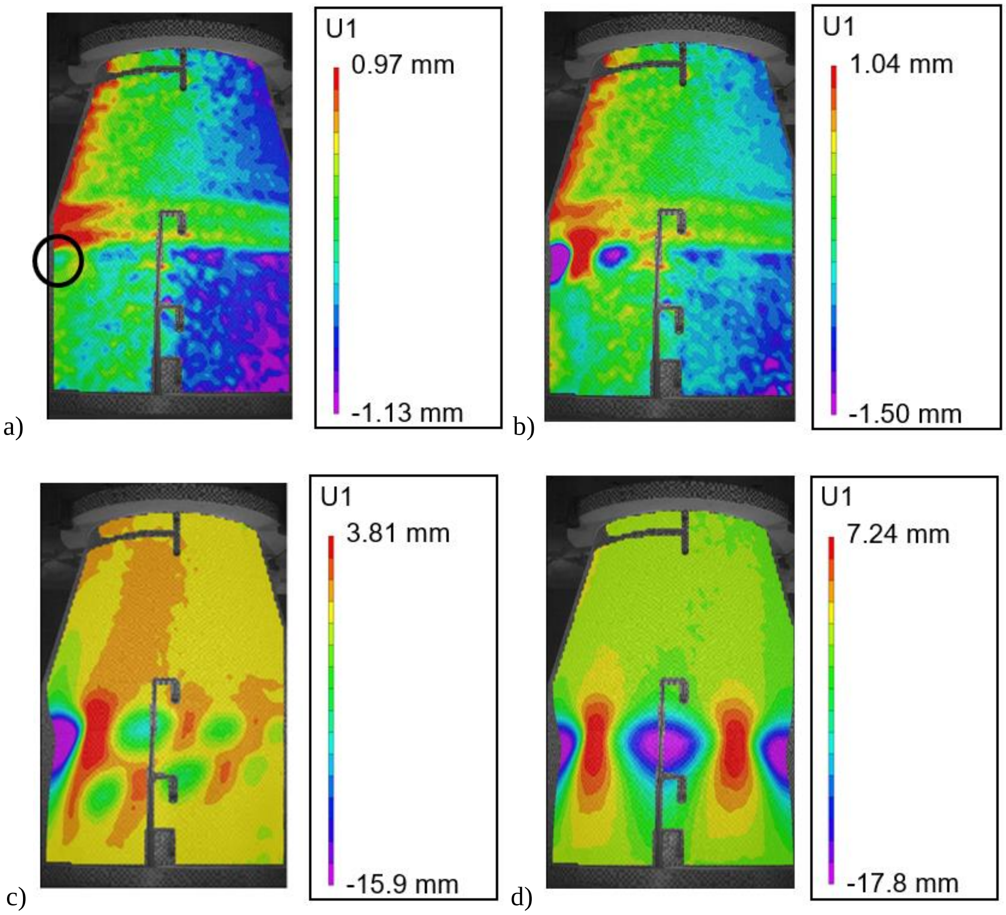

Figure 35. Buckling propagation from a) buckling initiation; b) 1.6 milliseconds after (a); c) 3.2 milliseconds after (a);and d) Postbuckling configuration.

.

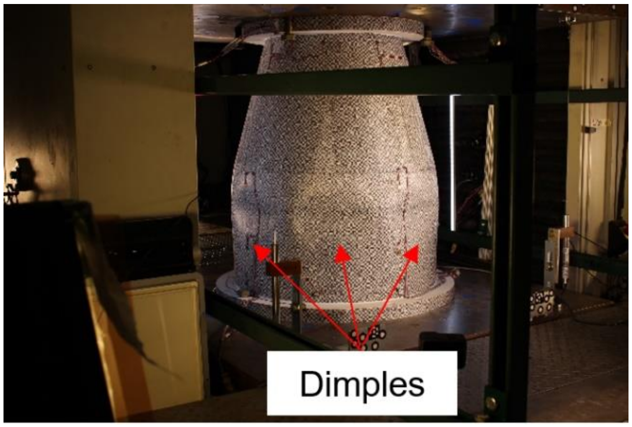

Figure 36. Postbuckling configuration of 3CHELL from the second test.

The maximum and minimum principal strain distributions at incipient buckling for the second buckling test is shown in Figure 37 and Figure 38, and are similar to that of the first buckling load sequence (Figure 23 and Figure 25). The contour plots for the measured maximum and minimum principal strain at incipient buckling from the second test are analogous to the first test. The areas of the most positive and most negative strain values occur in the transition region. The highest value for the maximum principal strain at incipient buckling for the second test was 2924 με, which is within 100 με of the first test, and the error limits of the DIC capability. The lowest value for the minimum principal strain incipient of buckling for the second test was -3546 με, which is approximately 10% lower than the first test (4222 με).

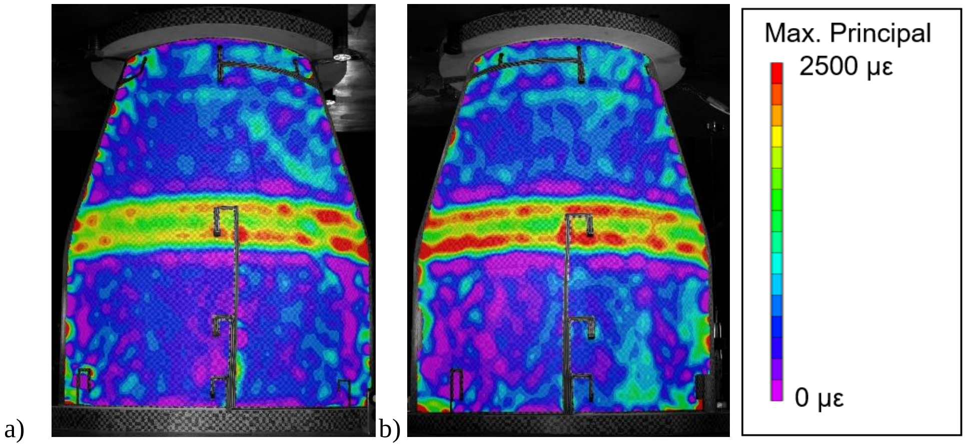

Figure 37. Measured maximum principal strain at incipient buckling: a) centered at 0 degrees; b) centered at 180 degrees.

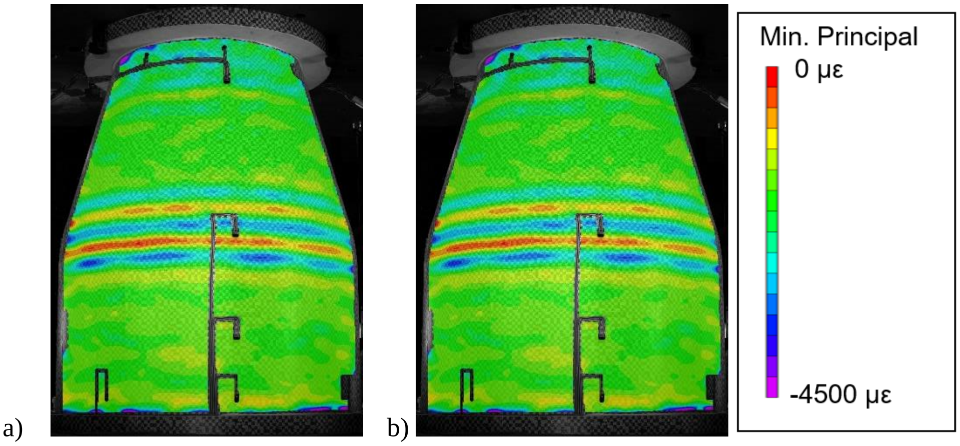

**Figure 38. Measured minimum principal strain at incipient buckling:
a) centered at 0 degrees; b) centered at 180 degrees.**

The maximum and minimum principal strains for the postbuckling configuration are very similar between the first, Figure 31 and Figure 33, and second tests, Figure 39 and Figure 40. The measured maximum principal strain from the second test is 9064 με, which is only 10 με different from the measured maximum principal strain from the first test (9055 με). The measured minimum principal strain from the second test is -9032 με and is approximately 600 με less than what was measured in the first test (-9613 με).

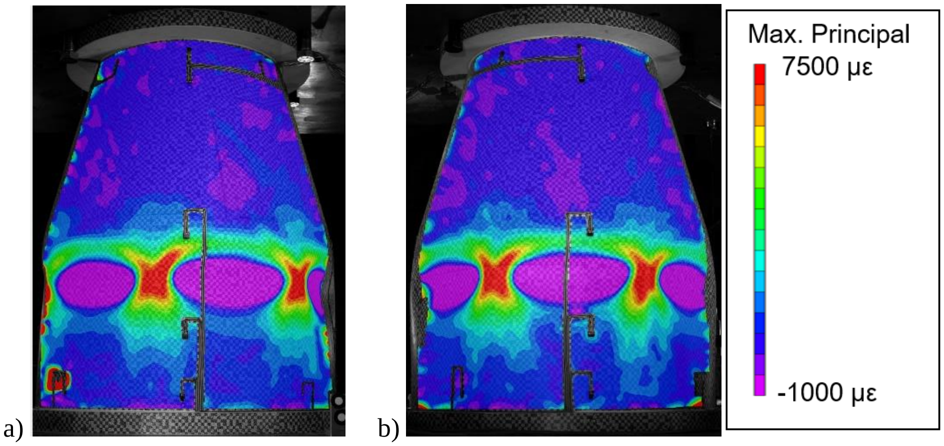

**Figure 39. Measured maximum principal strain at postbuckling:
a) centered at 0 degrees; b) centered at 180 degrees.**

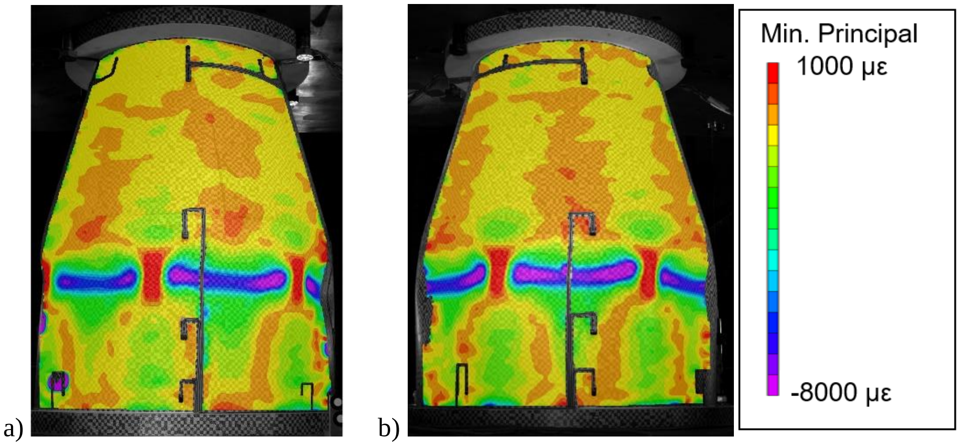

Figure 40. Measured maximum principal strain at postbuckling: a) centered at 0 degrees; b) centered at 180 degrees.

VI. Concluding Remarks

Utilizing a single-piece composite conical-cylindrical shell with a toroidal transition for aerospace applications has the potential to reduce structural mass and expand the design space for launch vehicles and payload adapters. This geometry combines cylindrical and conical shells common in launch vehicle architecture, thereby eliminating the need for the heavy, stiff interface ring that often separates two independent shell structures. However, such conical-cylindrical shells can be susceptible to stability failures. A composite conical-cylindrical shell with a toroidal transition, 3CHELL, was designed to fail in buckling, fabricated, and tested in an effort develop a better understanding the buckling response of this type of shell structure. The numerical and experimental data presented herein provide insight into the ability to predict the buckling response of a composite-conical cylindrical shell using nonlinear FEMs to aid in future design guidelines and recommendations for structures of this geometry.

The purpose of the presented work is to demonstrate the ability to predict the buckling behavior of this uncommon shape in order to influence the future designs of launch vehicles and payload adapters. A FEM that included radial imperfections and thickness variations was developed, and GNA analyses were conducted to predict the structural response. The test article buckled at 251.8 kN, and the predicted buckling load from an analysis which included measured off-nominal shear movement of the load platens was 231.4 kN, an 8.8% difference. The lateral displacement was 20% of the total axial end shortening at buckling but did not significantly influence the results. The predicted and measured buckling responses had several similarities when radial displacements and patterns at incipient buckling and postbuckling were compared. The measured and predicted buckling-initiation location were different, but similar patterns in the radial deformations and magnitudes could be identified. In addition, the buckling test was repeated since 3CHELL buckled without perceptible failure, and in the second test 3CHELL buckled within 1% of the first buckling test.

Some of the discrepancies, such as buckling load, buckling location, and test-article stiffness, between test and analysis may be attributable to the size of the test article and its design. For example, one possible explanation for the differences in stiffness, buckling load, and buckling location is the assumptions made when incorporating thickness variations due to ply overlaps in the conical region. The overlaps were a manufacturing limitation of the AFP robot to maintain a constant fiber angle along the length of the cone, while eliminating gaps. For a larger structure, these manufacturing limitations observed in 3CHELL may not be an issue, but all sources of stiffness variation should be included in the FEM since the buckling behavior of conical-cylindrical seems to be sensitive to stiffness variations.

Funding Sources

This testing was funded by the NASA MSFC Technical Excellence Fund.

Acknowledgments

The work described in this report was conducted in part with support of the NASA Engineering and Safety Center (NESC), in collaboration with the Delft University of Technology. The authors would like to thank the engineers and technicians in the MSFC Composite Technology Lab and the MSFC Structural Test Lab.

References

[1] National Aeronautics and Space Administration, "NASA's Space Launch System Reference Guide 2022," https://www.nasa.gov/sites/default/files/atoms/files/sls_reference_guide_2022_print_0.pdf, accessed November 2022.

[2] National Aeronautics and Space Administration. "Universal Stage Adapter." https://www1.grc.nasa.gov/space/usa/, last accessed on November 2022.

[3] European Space Agency, "Deploying Multiple Satelites with Syla and Vespa," https://www.esa.int/Enabling_Support/Space_Transportation/Deploying_multiple_satellites_with_Sylda_and_Vespa, last accessed on November 2022.

[4] Weingarten V.I., Seide P., Peterson J.P., "Buckling of Cylindrical Shells," NASA Space Vehicle Design Criteria (Structures), NASA SP-8007, 1965.

[5] Hilburger M.W., Starnes J.H., Jr., “Effects of Imperfections of the Buckling Response of Composite Shells,” Thin-Walled Structures, Vol. 42, 2004, pp.369-397. https://doi.org/10.1016/j.tws.2003.09.001.

[6] Takano A., Kitamura R., Masai T., and Bao J., "Buckling Test of Composite Cylindrical Shells with Large Radius Thickness Ratio." Applied Sciences, Vol. 11, No. 2, 2021, 854. https://doi.org/10.3390/app11020854.

[7] Rudd M.T., Eberlein D.J., Waters W.A., Gardner N.W, Schultz M.R, Bisagni C., “Analysis and Validation of a Scaled, Launch-Vehicle-Like Composite Cylinder under Axial Compression,” Composite Structures, Vol. 304, Part 1, 2023, 116393. https://doi.org/10.1016/j.compstruct.2022.116393.

[8] Hartwich T.S., Panek S., Wilckens D., Bock M., and Krause D., "The Influence of the Manufacturing Process and Test Boundary Conditions on the Buckling Load of Thin-Walled Cylindrical CFRP shells," Composite Structures, Vol. 308, 2023, 116674. https://doi.org/10.1016/j.compstruct.2023.116674.

[9] Wagner H. N. R., Huhne C., Niemann S., “Robust Knockdown Factors for the Design of Axially Loaded Cylindrical and Conical Composite Shells- Development and Validation,” Journal of Composite Structures, Vol. 173, 2017, pp. 281-303. https://doi.org/10.1016/j.compstruct.2017.02.031.

[10] European Commission, “Final Report Summary - DESICOS (New Robust DESIgn Guideline for Imperfection Sensitive Cmposite Launcher Structures),” FP&-SPACE-2011-282522, https://cordis.europa.eu/project/id/282522/reporting, accessed February 2023.

[11] Schultz M.R., Sleight D.W., Gardner N.W., Rudd M.T., Hilburger M.W., Palm T., Oldfield N.J.. “Test and Analysis of a Buckling-Critical Large-Scale Sandwich Composite Cylinder,” AIAA 2018-1693, AIAA SciTech 2018 Forum, Orland, Florida; 2018. https://doi.org/10.2514/6.2018-1693.

[12] Przekop A., Schultz M.R., Kosztowny C.J.R., Gardner N.W., Song K., Rudd M.T., “Buckling Test and Analysis of the 8-Foot-Diameter Sandwich Composite Cylinder Test Article CTA8.2 as part of the Shell Buckling Knockdown Factor Project: Test dates 5-7 December 2017 NASA/TM-20210024095, 2022.

[13] Song K., Schultz M.R., Kosztowny C.J.R., Gardner N.W., Rudd M.T., “Buckling Test and Analysis of the 8-Foot-Diameter Sandwich Composite Cylinder Test Article CTA8.3 as part of the Shell Buckling Knockdown Factor Project: Test dates 16-19 December 2019,” NASA-TM-20210024768, 2021.

[14] Weingarten V.I., Seide P., “Buckling of Thin-Walled Truncated Cones.” NASA Space Vehicle Design Criteria (Structures), NASA SP-8019, 1968.

[15] Tong L., “Buckling of Filament-Wound Laminate Conical Shells Under Axial Compression.” AIAA Journal , Vol. 37, No. 6, 1999, pp 778-781. https://doi.org/10.2514/2.792.

[16] Goldfeld Y., and Arbocz J., "Buckling of Laminated Conical Shells Given the Variations of the Stiffness Coefficients," AIAA Journal, Vol. 42, no. 3, 2004, pp. 642-649. https://doi.org/10.2514/1.2765.

[17] Khakimova R., Wilckens D., Reichardt J., Zimmermann R., Degenhardt R., "Buckling of Axially Compressed CFRP Truncated Cones: Experimental and Numerical Investigation," Journal of Composite Structures, Vol. 146, 2016, pp. 232-247. https://doi.org/10.1016/j.compstruct.2016.02.023.

[18] Khakimova R., Zimmermann R.,Wilckens D., Rohwer K., and Degenhardt R., "Buckling of Axially Compressed CFRP Truncated Cones with Additional Lateral Load: Experimental and Numerical Investigation," Composite Structures, Vol. 157, 2016, pp. 436 – 447. doi: https://doi.org/10.1016/j.compstruct.2016.08.011.

[19] Abramovich H., Kalnins K., Wieder A., "Test Results on the Stability and Vibrations of Composite Shells," *Stability and Vibrations of Thin-Walled Composite Structures*. Woodhead Publishing, Sawston, Cambridge, 2017, pp. 619-691.

[20] Sleight D.W., Satyanarayana A., Li Y., and Schultz M.R., "Buckling Imperfection Sensitivity of Conical Sandwich Composite Structures for Launch-Vehicles," AIAA 2021-1696, AIAA SciTech 2018 Forum Orlando, FL, January 2018. https://doi.org/10.2514/6.2018-1696.

[21] Wunderluich W., Obrecht H., Springer H., Lu Z., "A Semi-Analytical Approach to the Nonlinear Analysis of Shells of Revolution," Analytical and Computational Models for Shells, ASME Winter Annual Meeting, 1989.

[22] Anwen, W., "Stresses and Stability for the Cone-Cylinder Shells with Toroidal Transition," International Journal of Pressure Vessels and Piping, Vol. 75, No. 1, 1998, pp. 49–56. https://doi.org/10.1016/S0308-0161(98)00013-1.

[23] Patel B.P., Nath, Y., and Shukla, K.K., "Nonlinear Thermo-Elastic Buckling Characteristics of Cross-Ply Laminated Joined Conical- Cylindrical Shells," International Journal of Solids and Structures, Vol. 43, No. 16, 2006, pp. 4810–4829. https://doi.org/10.1016/j.ijsolstr.2005.07.025.

[24] Singh S., Patel B.P., and Nath Y., "Postbuckling Behavior of Angle-Ply Laminated Joined Circular Conical-Cylindrical Shells," American Institute of Aeronautics and Astronautics Journal, Vol. 45, No. 4, 2007, pp. 942–949. https://doi.org/10.2514/1.28358

[25] Zareim M., Rahimi G.H., "Buckling Resistance of Joined Composite Sandwich Conical-Cylindrical Shells with Lattice Core Under Lateral Pressure," Thin-Walled Structures, Vol. 174, 2022, 109027. https://doi.org/10.1016/j.tws.2022.109027.

[26] Hu W.C.L., Raney J.P., "Experimental and Analytical Study of Vibrations of Joined Shells," AIAA Journal, Vol. 5, No. 5, May 1967, pp. 976-980. https://doi.org/10.2514/3.4111.

[27] Bushnell D., Galletly G.D., "Comparisons of Test and Theory for Nonsymmetric Elastic-Plastic Buckling of Shells of Revolution." International Journal of Solids Structures, Vol. 10, 1974, pp. 1271-1286. https://doi.org/10.1016/0020-7683(74)90072-9.

[28] Zhao Y., "Buckling Behaviour of Imperfect Ring-Stiffened Cone–Cylinder Intersections Under Internal Pressure," International Journal of Pressure Vessels and Piping, Vol. 82, No. 7, 2005, pp. 553–564. https://doi.org/10.1016/j.ijpvp.2005.01.008.

[29] Chronopoulos D., Ichchou M., Troclet B., Bareille O., "Predicting the Broadband Response of Layered Cone-Cylinder-Cone Shell," Journal of Composite Structures, Vol. 107, 2014, pp. 149-159. http://dx.doi.org/10.1016/j.compstruct.2013.07.055.

[30] Marguerre K., "Stability of the Cylindrical Shell of Variable Curvature," Technical Memorandum, NACA TM 1302, 1951.

[31] Baker E. H., Cappelli A. P., Kovalevsky L., Rish F. L., Verette R. M., "Shell Analysis Manual," NASA Contractor Report, NASA CR- 192, 1968.

[32] Almroth B. O., Bushnell D., Sobel L. H., "Buckling of Shells of Revolution with Various Wall Constructions: Volume 1- Numerical Results," NASA Contractor Report, NASA CR- 1049, 1968.

[33] Bushnell D., Almroth B. O, Sobel L. H., "Buckling of Shells of Revolution with Various Wall Constructions: Volume 2- Basic Equations and Method of Solution," NASA Contractor Report, NASA CR- 1050, 1968.

[34] Tornabene, F., Viola, E., "Static Analysis of Functionally Graded Doubly-Curved Shells and Panels of Revolution," Meccanica, Vol. 48, 2013, pp. 901-930 https://doi.org/10.1007/s11012-012-9643-1.

[35] Tornabene, F., Fantuzzi, N., Bacciochi, M., "Free Vibrations of Free-Form Doubly-Curved Shells Made of Functionally Graded Materials using Higher-Order Equivalent Single Layer Theories," Composites: Part B, Vol. 67, 2014, pp. 490-509. https://doi.org/10.1016/j.compositesb.2014.08.012.

[36] Zingoni A., Enoma., "Strength and Stability of Spherical-Conical Shell Assemblies Under External Hydrostatic Pressure," Thin-Walled Structures, Vol. 146, 2020, 106472. https://doi.org/10.1016/j.tws.2019.106472.

[37] Clarkson E., "Hexcel 8552 IM7 Unidirectional Prepreg 190 gsm & 35%RC Qualification Statistical Analysis Report," Technical Report NCP-RP-2009-028 Rev B; 2019.

[38] Metallic Materials Properties Development and Standardization (MMPDS), vol. 10, April 2015.

[39] Micor Micorox® Standard Grout Data Sheet, https://www.micorco.com/wp-content/uploads/2014/03/Micorox-Standard-Grout-PDF-3-2014.pdf, last accessed November 2022.

[40] Alexander B.F., Ng K.C., "3D. Shape Measurement by Active Triangulation Using an Array of Coded Light Stripes," SPIE: Optics, Illumination and Image Sensing for Machine Vision II, Vol. 850, 1988, pp. 199–209. doi:10.1117/12.942878

[41] Bomarito G.F., Hochhalter J.D., Ruggles T.J., Cannon A.H., "Increasing Acuracy and Precision of Digital Image Correlation Through Pattern Optimization," Optics and Lasers in Engineering, Vol. 91, 2017, pp. 73-85. https://doi.org/10.1016/j.optlaseng.2016.11.005.

[42] Bomarito G.F., Hochhalter J.D., Ruggles T.J.,"Development of Optimal Multiscale Patterns for Digital Image Correlation via Local Grayscale Variation," Experimental Mechanics, Vol. 58, 2018, pp. 169-1180. https://doi.org/10.1117/12.942878.

[43] ABAQUS/Standard User's Manual. Version 2021 ABAQUS. Inc. USA; 2021.

[44] Blom A.W., Tatting B.F., Hol J.M.A.M., Gurdal, Z., “Fiber Path Definitions for Elastically Tailored Conical Shells” Composites Part B: Engineering; Vol. 40, 2009, pp. 77-84. https://doi.org/10.1016/j.compositesb.2008.03.011.

[45] Kosztowny C. J. R., “Implementing Geometric Surface Imperfections into Sandwich Composite Cylinder Finite Element Method Models,” AIAA 2021-0439, AIAA SciTech 2021 Forum, January 2021. https://doi.org/10.2514/6.2021-0439.